Systems/Circuits

An ErbB4-Positive Neuronal Network in the Olfactory Bulb for Olfaction

Zhibing Tan,[1*] Zhipeng Liu,[1*] Yu Liu,[1] Fang Liu,[2] Heath Robinson,[1] Thiri W. Lin,[2] Wen-Cheng Xiong,[1,3] and Lin Mei[1,3]

[1]Department of Neurosciences, Case Western Reserve University, School of Medicine, Cleveland, Ohio 44106, [2]Department of Neuroscience and Regeneration Medicine, Medical College of Georgia, Augusta University, Augusta, Georgia 30912, and [3]Louis Strokes Cleveland Veterans Affairs Medical Center, Cleveland, Ohio 44016

Olfactory information is relayed and processed in the olfactory bulb (OB). Mitral cells, the principal output excitatory neurons of the OB, are controlled by multiple types of interneurons. However, mechanisms that regulate the activity of OB interneurons are not well understood. We provide evidence that the transmembrane tyrosine kinase ErbB4 is selectively expressed in subsets of OB inhibitory neurons in both male and female mice. ErbB4-positive (ErbB4$^+$) neurons are mainly located in the glomerular layer (GL) and granule cell layer (GCL) and do not express previously defined markers. Optogenetic activation of GL-ErbB4$^+$ neurons promotes theta oscillation, whereas activation of those in the GCL generates γ oscillations. Stimulation of OB slices with NRG1, a ligand that activates ErbB4, increases GABA transmission onto mitral cells, suggesting a role of OB NRG1-ErbB4 signaling in olfaction. In accord, ErbB4 mutant mice or acute inhibition of ErbB4 by a chemical genetic approach diminishes GABA transmission, reduces bulbar local field potential power, increases the threshold of olfactory sensitivity, and impairs odor discrimination. Together, these results identified a bulbar inhibitory network of ErbB4$^+$ neurons for olfaction. Considering that both *Nrg1* and *Erbb4* are susceptibility genes for neuropsychiatric disorders, our study provides insight into pathologic mechanisms of olfactory malfunctions in these disorders.

Key words: **ErbB4; interneuron; local field potential; olfaction; olfactory bulb**

Significance Statement

This study demonstrates that ErbB4$^+$ neurons are a new subset of olfactory bulb inhibitory neurons in the glomerular layer and granule cell layer that innervate mitral cells and ErbB4$^-$ cells. They regulate olfaction by controlling local synchrony and distinct oscillations. ErbB4 inhibition diminishes GABA transmission, reduces bulbar local field potential power, increases the threshold of olfactory sensitivity, and impairs odor discrimination. Our results provide insight into pathophysiological mechanism of olfaction deficits in brain disorders associated with *Nrg1* or *Erbb4* mutations.

Introduction

Olfaction enables us to detect odorants in the external environment (Ache and Young, 2005; Hu et al., 2007). Odorants bind to olfactory receptors of olfactory sensory neurons (OSNs) in the nasal epithelium, which send the signal to the olfactory bulb (OB) (Firestein, 2001; Nagayama et al., 2014). In the OB, axons of OSNs synapse onto interneurons and dendrites of mitral cells (MCs), the principal output excitatory neurons of the OB. Axons of MC form the olfactory tracts and transfer information to various brain regions, including the piriform cortex and amygdala. In addition, the OB is a primary processing center of olfactory information (Ressler et al., 1994; Mori et al., 1999). MC output is controlled by multiple types of interneurons in the OB, which outnumber excitatory neurons by 100:1, in sharp contrast to 1:5 in the brain (Lledo et al., 2008). Evidence indicates that inhibitory neurons in the OB increase the signal-to-noise ratio, shaping MC spike patterns, synchronizing MC spike timing, and sharpening odor representations (Gire and Schoppa, 2009; Cleland and Linster, 2012; Najac et al., 2015).

GABAergic interneurons in the OB are heterogeneous in electrophysiological properties, morphology, and biomarkers; each subtype may form circuits with different functions (Lledo et al., 2008; Nagayama et al., 2014). They express tyrosine hydroxylase

Received Jan. 17, 2022; revised June 17, 2022; accepted June 27, 2022.

Author contributions: Z.T., W.-C.X., and L.M. designed research; Z.T., Z.L., Y.L., F.L., and T.W.L. performed research; Z.T. and H.R. analyzed data; Z.T. wrote the first draft of the paper; Z.T., Y.L., and L.M. edited the paper; Z.T. and L.M. wrote the paper.

This work was supported by the National Institutes of Health to L.M. and W.-C.X.; and Veterans Affairs to L.M. and W.-C.X. Contact for reagent and resource sharing: Further information and requests for reagents and resources should be directed to and will be fulfilled by corresponding author. The data that support the findings of this study are available from the corresponding author upon reasonable request. Source files are provided.

*Z.T. and Z.L. contributed equally to this work.

The authors declare no competing financial interests.

Correspondence should be addressed to Lin Mei at lin.mei@case.edu.

https://doi.org/10.1523/JNEUROSCI.0131-22.2022

(TH), calbindin (CB), parvalbumin (PV), calretinin (CR), and a combination of these molecules (Kiyokage et al., 2010; Nagayama et al., 2014). Based on the location, bulbar interneurons can be classified into periglomerular (PG) cells in the glomerular layer (GL), granule cells (GC) in the granule cell layer (GCL), and short axon (SA) cells across the entire OB (Nagayama et al., 2014). Odor representation is regulated by intraglomerular and interglomerular inhibition mediated by different interneurons (Aungst et al., 2003; Fukunaga et al., 2014; Economo et al., 2016). Specifically, PG cells synapse onto intraglomerular dendrites of MCs and provide ~50% of inhibitory inputs, critical to intraglomerular inhibition (Pinching and Powell, 1971; Toida et al., 1998; Dong et al., 2007; Kosaka and Kosaka, 2007). GCs synapse onto secondary dendrites of MCs, which is important for interglomerular inhibition (Urban and Sakmann, 2002; Schoppa, 2006). Intraglomerular circuits are activated by the respiratory cycle and regulate the baseline of odor-evoked inhibition for theta activity in the OB, whereas interglomerular circuits orchestrate γ synchrony and spike timing (Fukunaga et al., 2014; Najac et al., 2015). PV^+ interneurons and GCs form reciprocal synapses with the secondary dendrites of MC; they are activated by MCs and, in turn, inhibit MCs (Toida et al., 1994, 1996; Yokoi et al., 1995; Isaacson and Strowbridge, 1998; Schoppa et al., 1998; Christie et al., 2001; Huang et al., 2013; Kato et al., 2013; Miyamichi et al., 2013). However, the precise function of these local inhibitory networks remains elusive because of the vast heterogeneity of interneurons. In addition, little is known about molecular mechanisms that regulate the activity of the inhibitory circuits.

Here, we provide evidence that the transmembrane tyrosine kinase ErbB4 is a marker of PGs and GCs that seldomly coexpress known markers of OB interneurons. Layer-specific optogenetics activation of $ErbB4^+$ neurons promotes oscillatory activities through increasing local spike-phase locking. Neuregulin-1 (NRG1), a ligand that activates ErbB4, increases GABA transmission onto MCs, suggesting a role of NRG1-ErbB4 signaling in olfaction. In agreement, we found that ErbB4 mutant mice are impaired in GABA transmission, bulbar local field potential (LFP) power, and olfaction. Finally, by a chemical genetic approach, we demonstrated that acute inhibition of ErbB4 kinase impairs olfaction by reducing LFP powers. Together, our results identified a bulbar inhibitory network of $ErbB4^+$ neurons for olfaction. Considering that both *Nrg1* and *Erbb4* are susceptibility genes for neuropsychiatric disorders (Mei and Xiong, 2008; Shi et al., 2009; Mei and Nave, 2014; Howard et al., 2019), our study provides potential mechanisms of olfactory malfunctions in these disorders.

Materials and Methods

Animals. Mice were maintained on a 12 h light-dark cycle with *ad libitum* access to food and water. Both male and female mice, 2-5 months of age, were used in the study. ErbB4 null mutant mice were crossed with *αMHC-ErbB4* transgenic mice that express ErbB4 in the heart to generate *ErbB4 null; αMHC-ErbB4* ($ErbB4^{-/-}$) mice that were described previously (Tidcombe et al., 2003). *ErbB4 T796G* knock-in mice were generated by homologous recombination as described previously (Tan et al., 2018). The primers for genotyping WT Erbb4 allele were as follows: forward, 5′-GATCTGCAGATCAATTCAC-3′, reverse, 5′-GCCAACCAACTGGATAGTG-3′. The primers for genotyping the *T796G ErbB4* allele were as follows: forward, 5′-AACTGAATTCACTT TGTGG-3′, reverse, 5′-CTGTAGCAGCAACAATAGC-3′. Mice were maintained as homozygotes in a mixed 129S6 and C57BL/6J background.

ErbB4-Ai9 mice were generated by crossing *ErbB4-CreER*^{T2} mice (The Jackson Laboratory, stock #012360) with *Ai9* mice (The Jackson Laboratory, stock #007909). *ErbB4-ChR2* mice were generated by crossing *ErbB4-Ai9* mice with *Ai32* mice (The Jackson Laboratory, stock #012569). In *ErbB4-CreER*^{T2} mice, the endogenous *ErbB4* gene is intact and $CreER^{T2}$ fusion protein is expressed under the control of the endogenous promoter/enhancer regions of the *ErbB4* gene. *Ai9* mice express robust tdTomato fluorescence following Cre-mediated recombination. *Ai32* mice carry an improved channelrhodopsin-2/EYFP fusion protein (ChR2-EYFP) whose expression is restricted by a *floxed-STOP* cassette. All procedures were approved by Case Western Reserve University Institutional Animal Care and Use Committees.

Tamoxifen preparation and administration. Tamoxifen (20 mg) was dissolved in 0.5 ml ethanol; the solution was then added to 1 ml corn oil. After being vortexed, the mixture was placed in a 60°C incubator for ethanol to evaporate, for a final concentration of 20 mg/ml in corn oil. *ErbB4-Ai9* or *ErbB4-ChR2* mice were given tamoxifen at least 2 weeks before experiment, to induce Cre-mediated excision of the STOP signal in the *floxed-STOP* cassette, allowing tdTomato and/or ChR2-EYFP expressing in $ErbB4^+$ cells. In a typical regiment, mice were given tamoxifen via gavage at 20 mg/kg body weight once, or once every other day for 3 times, or once every week for 6 weeks (referred to as one dose, three doses and six doses, respectively).

Imaging. Brain sections were imaged under a confocal laser scanning microscope (Nikon A1R) or a BZ-X fluorescence microscope (Keyence). The energy of excitation light was adjusted for better fluorescence signals, except those to compare tamoxifen dose-dependent effects when the energy was kept consistent. Images were analyzed by Image-Pro Plus (version 6, Media Cybernetics). In brief, image data were split into individual color channels and transferred to an 8-bit gray format. Data were analyzed initially with a threshold that was generated automatically by the software based on the averaged fluorescence intensity of individual images. If necessary, software-generated thresholds were optimized to ensure that the largest number of cells were detected; further increase or reduction of the optimal thresholds could "convert" neuropils into somas or decrease the number of somas, respectively. Cell numbers and grayscale were calculated under the Count/Size and Measurements functions, respectively.

Electrode, fiber, and cannula implantation. Mice were anesthetized with ketamine/xylazine (Sigma, 0.1 ml/10 g body weight, i.p.), shaved on the skull, and positioned on a stereotaxic apparatus. After antiseptic treatment, the scalp was removed, and the exposed skull area was cleared using 1% H_2O_2. For *in vivo* recording, craniotomy was performed unilaterally above the right OB (4.2 mm anterior, 0.6 mm lateral, ventral depth of the electrode and optic fiber were adjusted based on experimental purpose, see below). Tetrodes were made from 13-μm-diameter platinum (with 10% iridium) fine wire (California Fine Wire) and were attached to a movable screw microdrive on a custom-designed 3D-printed frame. Skull screws were placed over the cerebellum as ground and reference. For optogenetics in combination of *in vivo* recording, four tetrodes were glued to a ferrule-bound optical fiber (Thorlabs, 200-μm-diameter core, 0.39 NA) where tetrodes were arrayed semi-circularly around the lateral edge of the fiber. To target GL-$ErbB4^+$ neurons, the tip of optical fiber is 300-500 μm longer than the tetrodes, such that, after implantation, the tip of optical fiber was on top of GL (3.1 mm ventral) while tips of tetrode were near the ML. To target GCL-$ErbB4^+$ neurons, the tip of optical fiber is 300-500 μm shorter than tetrodes, such that, after implantation, the tip of optical fiber was in the GCL (2.5 mm ventral) while tips of tetrodes were near the ML. For *in vivo* recording of $ErbB4^{-/-}$ and *T796G* mice, tips of tetrode were targeted to the GCL (1.2 mm ventral). For inhibitor 4-amino-1-tert-butyl-3-(1′-naphthylmethyl) pyrazolo[3,4-day]pyrimidine (1NM-PP1) local injection, a cannula (Plastic One, 20 gauge) was placed on the top of the OB. To verify the locations of tetrodes, thermolytic lesions were induced by electric current (50 μA, 20 s) at the end of recording, and brain samples were examined histologically for lesion locations. Data were discarded when tetrodes or optic fibers were not in correct locations.

In vivo *recording*. After surgery, mice were allowed for recovery at least 1 week before recording. Spikes and LFP signals were recorded simultaneously from the OB. Signals were amplified, bandpass filtered (0.5-1000 Hz for LFPs and 0.6-6 kHz for spikes), and digitized using the OmniPlex Neural Data Acquisition System (Plexon). LFPs were collected at a rate of 1 kHz, while spikes, detected at adjustable online thresholds, were collected at 40 kHz. Units were clustered using the offline sorter MClust (MClust-4.4, Redish) and analyzed with a semiautomated super paramagnetic clustering algorithm (SPC, B. Hasz). Super paramagnetic clustering is a nonparametric clustering method that is more appropriate for spike sorting when the numbers and structures of clusters of neurons are unknown (Blatt et al., 1996). Two principal components for sorting were voltage peak and energy from each channel (Spellman et al., 2015). Clusters were accepted, merged, or eliminated based on visual inspection of feature segregation, waveform distinctiveness and uniformity, stability across recording session, and interspike interval distribution (Spellman et al., 2015).

Optogenetics. For optogenetics in slices, photostimulation was delivered by 473 nm solid-state laser diodes. The stimulus duration for recording ErbB4$^+$ neurons were 5 s given at 0.1 Hz, and duration for recording ErbB4$^-$ neurons was 2 s given at 0.2 Hz, which was controlled by a stimulator (Master 8). The power density of the blue light was 15-20 mW/mm^2, measured with a power meter (Thorlab). Blue light pulses were delivered to the slices through a quartz fiber (200 mm diameter, custom-made); the estimated size of the projection area of the photostimulation onto the slice was 2-3 mm^2.

For optogenetics *in vivo*, blue light (488 nm) was delivered at 0.033 Hz (10 s on, 20 s off) from an LED light source (Plexon). The frequency of the light was controlled by a stimulator (Master 8). Light intensity was measured with a power meter (Thorlab) and adjusted based on experiment purpose. Data were compared before, during, and after light stimulus of the same animal independent of behavioral state.

LFP power analysis. LFP recordings were processed in Neuroexplorer (Nex Technologies). Fourier transform of LFPs was performed and data were then binned with bin size of the following:

$$\text{Bin Size} = \frac{1}{(2 \times \text{Maximum Frequency})}$$

and the number of bins equal to 2 times the number of frequency values, which was set to 1024 (Tan et al., 2018). Power spectrum data were calculated by normalizing auto-spectrum products so that the values are equal to the mean squared values from the rate histogram that were calculated from the overall data. Normalized data were then converted to logarithmic scale and filtered by Gaussian filter with bin size of 3.

Phase locking. We examined synchrony within the OB by testing whether the firing of bulbar neurons was modulated by, or phase-locked to, the phase of ongoing field potential oscillations. Bulbar LFPs were digitally filtered using a bandpass filter, with filter order equivalent to the sampling frequency, with a zero-phase delay (filtfilt in MATLAB) to isolate frequencies in intended bands (theta: 1-12 Hz, β: 12-30 Hz, low-γ: 30-60 Hz, high-γ: 60-100 Hz). Data were filtered by zero-phase delay filter both in the forward and reverse direction to avoid phase distortion and preserve temporal aspects (Oppenheim et al., 1999). Filtered data were converted to corresponding phases by the Hilbert transform (Hilbert function in MATLAB), which calculates real and imaginary parts of the data to obtain instantaneous amplitudes and phases at any given time point (Oppenheim et al., 1999). Phase-locking was quantified as the circular concentration of the resulting phase distribution, which was defined as the mean resultant length (MRL) of the phase angles. The MRL is an average vector calculated by dividing the summation of individual vectors from each phase that corresponds to each spike by the number of spikes. It has values between 0 and 1, with 0 indicating no phase-locking and 1 indicating exact phase-locking. The MRL was measured with circular statistics using the CircStats toolbox in MATLAB. Bulbar spikes at individual time points were assigned to the same local LFP phases from the Hilbert transform. Only neurons with >100 spikes were included in calculation to limit sample-size bias (Mukai et al., 2015; Tan et al., 2018).

Slice preparation. Mice (4-5 weeks old) were anesthetized with isoflurane and subjected to cardiac perfusion with ice-cold oxygenated (95% O_2 and 5% CO_2) ACSF before decapitation. Brains were removed rapidly and placed into ice-cold oxygenated ACSF containing the following (in mM): 110 choline Cl, 3.5 KCl, 0.5 $CaCl_2$, 7 $MgCl_2$, 1.3 NaH_2PO_4, 25 $NaHCO_3$, and 20 glucose. The OB was dissected; transverse slices (300 μm) were cut on a vibratome (VT1200, Leica) and allowed to recover at 32°C for 1 h before recording. The ACSF used for recovery and recording contained the following (in mM): 125 NaCl, 3.5 KCl, 2 $CaCl_2$, 1.3 $MgCl_2$, 1.3 NaH_2PO_4, 25 $NaHCO_3$, and 10 glucose. Individual slices were transferred to a submerged recording chamber and continuously perfused with the ACSF (3.0 ml/min) at 32°C. Slices were visualized under a microscope (IX51WI, Olympus) using infrared video microscopy and differential interference contrast optics.

Electrophysiology. ErbB4$^+$ neurons were visualized under the fluorescence microscope. MCs were identified based on location (in ML), size of cell body, and confirmed through backfilling with 1% biocytin and morphologic examination. Patch electrodes were made from borosilicate glass capillaries (B-120-69-15, Sutter Instruments) with a resistance in the range of 2.5-4 MΩ. The internal solution for IPSC recording contained the following (in mM): 100 $CsCH_3SO_3$, 40 CsCl, 10 HEPES, 4 $MgCl_2$, 4 Na_2ATP, 0.4 Na_3GTP, 10 Tris-phosphocreatine, and 0.2 EGTA. For mIPSC recording, TTX (1 μM), CNQX (20 μM), and DL-AP5 (50 μM) were added to the recording ACSF to block action potentials (APs) and glutamatergic transmission, respectively. For eIPSC recording, TTX was excluded. mEPSC was recorded with internal solution containing the following (in mM): 125 K-gluconate, 15 KCl, 10 HEPES, 4 $MgCl_2$, 4 Na_2ATP, 0.4 Na_3GTP, 10 Tris-phosphocreatine, and 0.2 EGTA. TTX (1 μM) and bicuculline (BMI, 10 μM) were added to the recording ACSF to block APs and GABAergic transmission, respectively. Recordings were made with an Axon 700A patch-clamp amplifier and 1320A interface (Molecular Devices). The signals were filtered at 2 kHz using amplifier circuitry, sampled at 10 kHz, and analyzed using Clampex 9.0 (Molecular Devices).

Behavioral analysis. Olfaction was tested based on spontaneous investigation of odor sources without reward. The principle is that, repeatedly present, the same stimulus causes habituation (reducing investigation time), and a following new stimulus leads to dishabituation (increasing investigation time). For the olfactory sensitivity test, mice were presented with swab-carried mineral oil (4 times) followed by increasing concentrations (10^{-6} to 10^{-1}, increase of 10) of octanal in mineral oil for 2 min, and scored for sniffing time. For the odor discrimination test, mice were presented with mineral oil (4 times) and 10^{-2} octanal (4 times) followed by the presentation of an odor mixture (10^{-2} octanal + 10^{-2} heptanal). Mice were scored for 2 min for sniffing when the noses of mice were positioned within a 2 cm radius circle the swab-tip. Behaviors were videotaped and blindly analyzed *post hoc*.

Chemicals and antibodies. The recombinant NRG1 was prepared as described previously (Huang et al., 2000; Woo et al., 2007). 1NM-PP1 (529581) and rabbit anti-TH antibody (AB152, 1:1000 dilution) were purchased from EMD Millipore. Rabbit anti-PV antibody (PV25, 1:1000 dilution), mouse anti-CR antibody (010399, 1:500 dilution), and mouse anti-CB antibody (07(F), 1:500 dilution) were from Swant. Avidin AlexaFluor-488 conjugate (Avidin-488, A21370, 1:2000 dilution) was purchased from Thermo Fisher Scientific.

Statistical analyses. Two-tailed paired or unpaired Student's *t* test was used for analyzing datasets with two groups. Two-way ANOVA was used for datasets with repeated measures. Bonferroni correction was used for multiple comparisons. $p < 0.05$ is considered significant. Data are presented as mean ± SEM.

Results

ErbB4$^+$ neurons as a molecularly defined type of interneurons in the OB

To visualize ErbB4$^+$ neurons, *ErbB4-CreER^{T2}* (*ErbB4^{CreER}*) mice were crossed with *Rosa::LSL-tdTomato* (*Ai9*) mice where tdTomato expression is suppressed by a *lox-stop-lox* cassette. In *Erbb4^{CreER}*

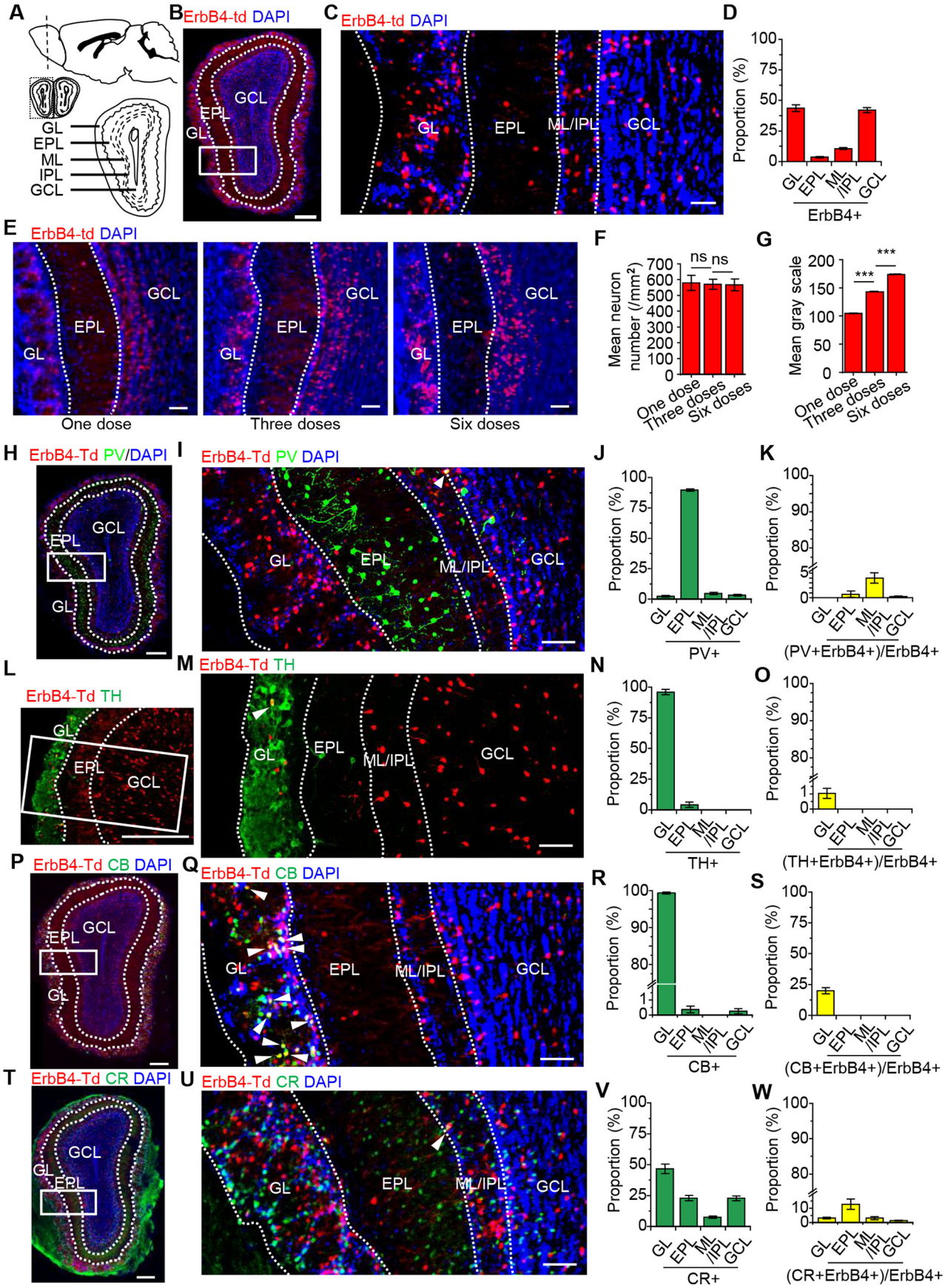

Figure 1. Unique distribution and marker expression of ErbB4$^+$ neurons in the OB. ***A***, Schematic diagram of the mouse brain (top) and layer structure of the OB (bottom). ***B***, Low-power confocal images represent the distribution of tdTomato-labeled ErbB4$^+$ neurons across the OB. ***C***, Zoomed view of the rectangle area of ***B***. ***D***, Summarized data showing the proportion of ErbB4$^+$ neurons in different layers ($n = 13$ images from 3 mice). ***E***, Confocal images represent the expression of tdTomato-labeled ErbB4$^+$ neurons under different tamoxifen dosages. Images

mice, the *Cre-ER^{T2}* cassette is inserted downstream of the *ErbB4* locus and does not alter the expression of endogenous ErbB4 (Madisen et al., 2010). The resulting *ErbB4-CreER^{T2};Ai9* (*ErbB4-Ai9*) mice were treated with tamoxifen (gavage, once every other day, ×3) to release the stop signal and thus enable the expression of tdTomato. Previous studies have demonstrated that tdTomato in *ErbB4-Ai9* mice faithfully identifies ErbB4$^+$ neurons because its expression is under the control of the endogenous promoter of the *Erbb4* gene (Madisen et al., 2010; Bean et al., 2014). The OB has a unique laminar structure, with five layers and from outside to inside: GL, external plexiform layer (EPL), mitral cell layer (ML), internal plexiform layer (IPL), and GCL (Nagayama et al., 2014). ErbB4$^+$ neurons were mainly distributed in the GL and GCL layers, which accounted for 43.7% and 42.1% of total ErbB4$^+$ cells in the OB. The ML/IPL contained 10.6% of ErbB4$^+$ neurons in the OB. ErbB4$^+$ neurons in the EPL were rare, merely ~3.6% (Fig. 1*A–D*). This distribution pattern of ErbB4$^+$ neurons is different from those of previously characterized bulbar interneurons (see below), suggesting that ErbB4 is expressed in a different group of interneurons in the OB. The distribution and number of tdTomato$^+$ cells were comparable in mice treated with once, 3 times, or 6 times with tamoxifen (for details, see Materials and Methods) (once vs three doses, $t_{(8)}$ = 0.16, p = 0.88; three doses vs 6 doses, $t_{(8)}$ = 0.08, p = 0.94, t test; Fig. 1*E,F*), although the fluorescence intensity was gradually increased (once vs three doses, $t_{(8)}$ = 38.1, $p < 0.001$; three doses vs 6 doses, $t_{(8)}$ = 21.4, $p < 0.001$, t test; Fig. 1*E,G*), suggesting that tdTomato labels a unique subset of interneurons, regardless of tamoxifen dosage. Unless otherwise indicated, mice were treated with 3 times tamoxifen. To characterize ErbB4$^+$ neurons, OB sections were stained with antibodies against established markers of OB interneurons: PV, TH, CB, and CR. As shown in Figure 1*H–J*, 89.7% of PV$^+$ neurons in the OB were confined in the EPL layer with occasional distribution in other layers, agreeing with previous reports (Kato et al., 2013). This distribution pattern contrasted with that of ErbB4$^+$ cells. In addition, <5% of ErbB4$^+$ cells in any given layer were positive for PV (Fig. 1*H–K*). These results indicate that most ErbB4$^+$ neurons in the OB are not PV$^+$, unlike those in the cortex and hippocampus, 65% of which were positive for PV (Bean et al., 2014). TH and CB are markers of PG neurons which are localized in the GL (Fig. 1*L–S*). Quantitatively, an overwhelming majority, ~95.9%, of TH$^+$ and ~99.4% of CB$^+$ neurons were located in the GL, but not other layers, in agreement with the literature (Toida et al., 1998; Kiyokage et al., 2010). Of ErbB4$^+$ neurons in the GL, 99% of ErbB4$^+$ neurons were negative for TH, although 19.9% were positive for CB (Fig. 1*L–S*). Unlike other markers, CR is not layer-specific (Fig. 1*T–W*); nevertheless, ErbB4$^+$ neurons that were positive for CR were 3.1% in GL, 3% in ML/IPL, 1.4% in GCL, and ~12.7% in EPL where ErbB4$^+$ neurons were sparse (Fig. 1*T–W*). Together, these results demonstrate that ErbB4$^+$ neurons represent a different type of molecularly defined neurons in the OB.

Bulbar ErbB4$^+$ neurons are PG and GC neurons with distinct morphologic and electrophysiological properties

To characterize ErbB4$^+$ neurons in GL and GCL, we first examined their morphology. The dense population of tdTomato$^+$ (i.e., ErbB4-td) cells in *ErbB4-Ai9* mice prevented morphologic characterization. Thus, they were patched individually and backfilled with 1% biocytin, which was visualized by Avidin-488 staining. As shown in Figure 2*A*, *B*, ErbB4$^+$ neurons in GL (GL-ErbB4$^+$ hereafter) had an extensive arborization of dendrites that were restricted within the GL, a typical morphology of PG cells (McQuiston and Katz, 2001; Figueres-Onate et al., 2014). Next, we studied the electrophysiological properties of GL-ErbB4$^+$ neurons by patch-clamp recording in whole-cell configuration (Fig. 2*C*). Their resting membrane potentials were −58.9 ± 2.11 mV and input resistances were 485.8 ± 61.4 MΩ. The input resistances were lower than a recent report (Najac et al., 2015), probably because of the heterogeneous of PG neurons. They generated spontaneous APs without stimulation (Fig. 2*D*). The resting membrane potentials of some neurons were relatively steady while others were repetitively fluctuating (Fig. 2*D*), indicating that GL-ErbB4$^+$ neurons are heterogeneous. PG cells can be further divided into two subtypes: Type I PG cells that receive direct inputs from OSNs and Type II PG cells that are innervated by external tufted cells but not OSNs. Tufted cells are glutamatergic neurons that generate spontaneous bursts of APs (Imai, 2014; Nagayama et al., 2014). In agreement, the latencies of eEPSCs of GL-ErbB4$^+$ neurons (in response to stimulation of OSNs) averaged at 2.8 ± 0.24 ms and 4.7 ± 0.39 ms, like Type I and Type II PG cells, respectively ($t_{(18)}$ = 4.0, p = 0.004, t test; Fig. 2*E,F*). To characterize their excitability, GL-ErbB4$^+$ neurons were current-clamped and injected with 2 s stepping currents from −25 pA to 200 pA at 25 pA per step. AP production was increased by current injection up to 100 pA. However, when injected currents were >100 pA, GL-ErbB4$^+$ neurons were able to generate APs initially, but the firing could not be maintained afterward (Fig. 2*G,H*), resulting a bell-shaped input–output curve (Fig. 2*H*). These data suggest that GL-ErbB4$^+$ neurons maintain a high activity at rest and they are easy to fatigue with continuous stimulation. These characters resembled those of PG cells (McQuiston and Katz, 2001; Nagayama et al., 2014), suggesting GL-ErbB4$^+$ neurons are a group of PG cells.

Although somas of GCL-ErbB4$^+$ neurons were located in the GCL, they appeared to be axonless and extended dendrites into the EPL (Fig. 2*I,J*), a typical morphology of GCs (Kosaka and Kosaka, 2007; Kiyokage et al., 2010; Nagayama et al., 2014). The resting membrane potentials of GCL-ErbB4$^+$ neurons were −75.3 ± 4.53 mV and the input resistances were 443 ± 12.3 MΩ. Spontaneous APs could not be recorded in GCL-ErbB4$^+$ neurons (Fig. 2*K,L*), unlike GL-ErbB4$^+$ neurons. When stimulated with injected stepping currents (from −25 pA to 200 pA with the step of 25 pA), GCL-ErbB4$^+$ neurons reliably produced APs even at higher currents. This resulted in a linear input–output curve (Fig. 2*M,N*). These data suggest that GCL-ErbB4$^+$ neurons

←

at 1, 3, and 6 doses were obtained at optimal thresholds (for details, see Materials and Methods). ***F***, Summarized data showing the density of ErbB4$^+$ neurons under different tamoxifen dosages (n = 5 images from 3 mice). ***G***, Summarized data showing the fluorescence intensity of ErbB4$^+$ neurons under different tamoxifen dosages (n = 5 images from 3 mice). ***H***, Low-power confocal images represent the colocalization of ErbB4$^+$ neurons (red) with PV$^+$ neurons (green). ***I***, Zoomed view of the rectangle area of ***H***. ***J***, ***K***, Summarized data showing the proportion of PV$^+$ neurons (***J***) and the PV/ErbB4 double-positive neurons account for total ErbB4$^+$ neurons (***K***) in different layers (n = 13 images from 3 mice). ***L***, Low-power confocal images represent the colocalization of ErbB4$^+$ neurons (red) with TH$^+$ neurons (green). ***M***, Zoomed view of the rectangle area of ***L***. ***N***, ***O***, Summarized data showing the proportion of TH$^+$ neurons (***N***) and the TH/ErbB4 double-positive neurons account for total ErbB4$^+$ neurons (***O***) in different layers (n = 7 images from 3 mice). ***P***, Low-power confocal images represent the colocalization of ErbB4$^+$ neurons (red) with CB$^+$ neurons (green). ***Q***, Zoomed view of the rectangle area of ***P***. ***R***, ***S***, Summarized data showing the proportion of CB$^+$ neurons (***R***) and the CB/ErbB4 double-positive neurons account for total ErbB4$^+$ neurons (***S***) in different layers (n = 13 images from 3 mice). ***T***, Low-power confocal images represent the colocalization of ErbB4$^+$ neurons (red) with CR$^+$ neurons (green). ***U***, Zoomed view of the rectangle area of ***T***. ***V***, ***W***, Summarized data showing the proportion of CR$^+$ neurons (***V***) and the CR/ErbB4 double-positive neurons account for total ErbB4$^+$ neurons (***W***) in different layers (n = 12 images from 3 mice). Scale bars: low-power image, 500 μm; zoomed view, 50 μm. ***$p < 0.001$.

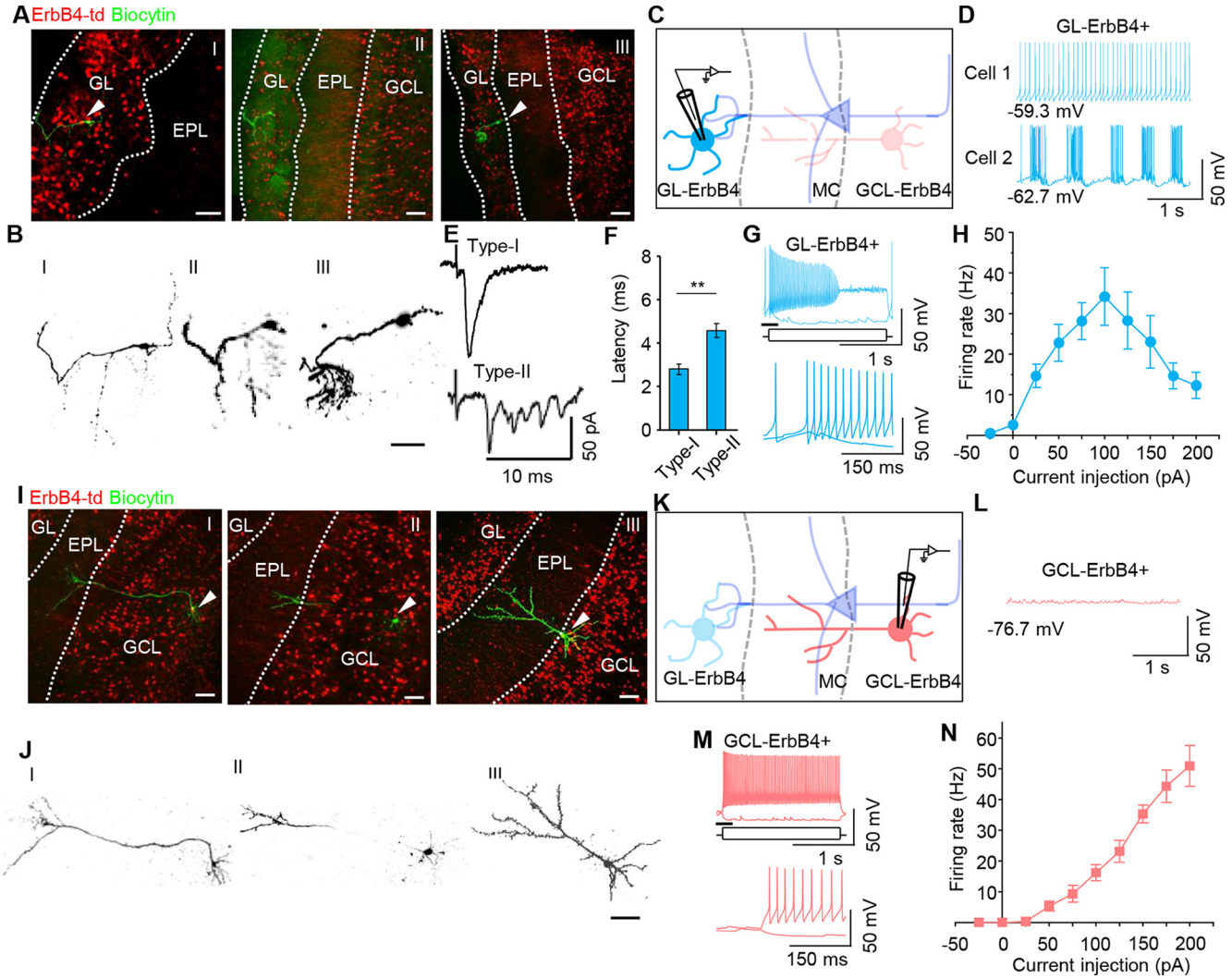

Figure 2. Morphologic and electrophysiological properties of ErbB4$^+$ neurons. ***A***, Confocal images represent the morphology of biocytin-labeled GL-ErbB4$^+$ neurons. ***B***, Grayscale images converted from ***A***, showing arborization of GL-ErbB4$^+$ neurons. ***C***, Schematic diagram showing the electrophysiological recording paradigm of ErbB4$^+$ neurons in GL. ***D***, Representative traces showing the resting membrane potential and spontaneous activities of GL-ErbB4$^+$ neurons ***E***, Representative traces of eEPSCs recorded from GL-ErbB4$^+$ neurons (OSN stimulation). ***F***, Summary of the latency of eEPSCs ($n = 7$ for short latency, $n = 13$ for long latency). ***G***, Top, Representative traces of GL-ErbB4$^+$ neurons in responding to step current injection. Bottom, Zoom view of the first 0.3 s of top trace. ***H***, Input–output curve showing the excitability of GL-ErbB4$^+$ neurons ($n = 10$ from 3 mice). ***I***, Confocal images represent the morphology of biocytin-labeled GCL-ErbB4$^+$ neurons. ***J***, Grayscale images converted from ***I***, showing arborization of GCL-ErbB4$^+$ neurons. ***K***, Schematic diagram showing the electrophysiological recording paradigm of ErbB4$^+$ neurons in GCL. ***L***, Representative traces showing the resting membrane potential and spontaneous activities of GCL-ErbB4$^+$ neurons. ***M***, Top, Representative traces of GCL-ErbB4$^+$ neurons in responding to step current injection. Bottom, Zoom view of the first 0.3 s of top trace. ***N***, Input–output curve showing the excitability of GCL-ErbB4$^+$ neurons ($n = 8$ from 3 mice). $^{**}p < 0.01$.

were silent at rest and could faithfully respond to continuous stimulation. Thus, we have demonstrated that bulbar ErbB4$^+$ neurons are PG and GC neurons with distinct morphologic and electrophysiological properties.

GL-ErbB4$^+$ and GCL-ErbB4$^+$ neurons form inhibitory synapses onto MCs

To identify the downstream target neurons of ErbB4$^+$ neurons, we sought to activate them by optogenetics. *ErbB4-Ai9* mice were crossed with *ChR2 flox/flox* mice (*Ai32*); resulting *ErbB4-ChR2* mice (i.e., *ErbB4-CreER^{T2};Ai9;Ai32*) expressed ChR2 specifically in ErbB4$^+$ neurons. ChR2 is a light-driven nonselective cation channel that enables robust and reversible photostimulation of neuronal AP firing (Boyden et al., 2005). Light stimulation (blue, 488 nm) of OB slices from *ErbB4-ChR2* mice elicited inward currents (Fig. 3*A*,*B*) and induced APs in ErbB4$^+$ neurons in GL and GCL (Fig. 3*A*,*B*). The firing patterns of GL- and GCL-ErbB4$^+$ neurons by optogenetic stimulation were similar to current injections-induced APs (Fig. 2*G*,*M*). GL-ErbB4$^+$ cells produced APs within first few seconds but failed to generate APs afterward, whereas GCL-ErbB4$^+$ cells fired continuously during the 5 s period of stimulation (Fig. 3*A*,*B*). These results demonstrate that GC- and GCL-ErbB4$^+$ neurons could be activated by optogenetics.

Next, we attempted to identify the target cells of GL- and GCL-ErbB4$^+$ neurons. Cells in the GL, such as PG cells, form dendrodendritic inhibitory synapses in glomeruli onto apical dendrites of MCs, whereas cells in the GCL, such as GCs, synapse onto secondary dendrites of MCs (Yokoi et al., 1995; Nagayama et al., 2014). Therefore, we recorded MCs which were identified through location and verified by morphology after biocytin backfilling (Fig. 3*C*). We found blue light (488 nm) stimulation induced a serial of inward PSCs in MCs (Fig. 3*D*). The latency from light-on to the initiation of the PSCs was 3.7 ± 0.28 ms,

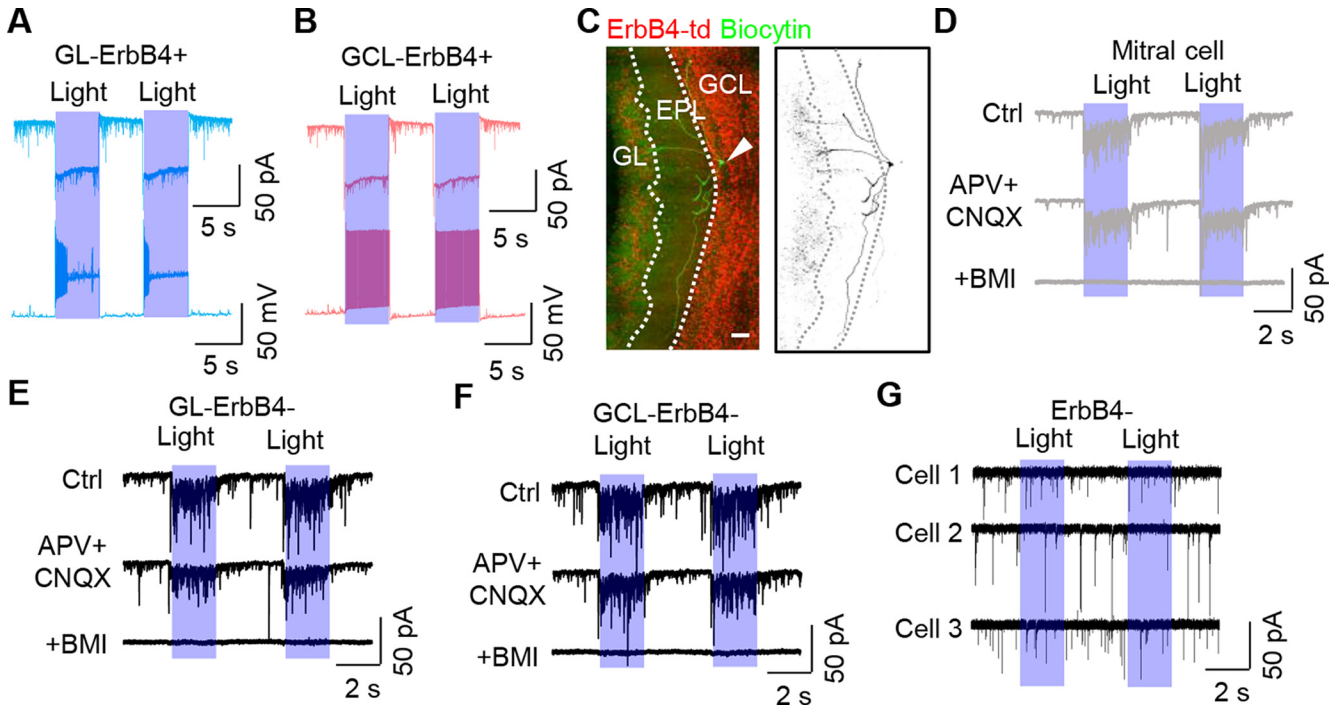

Figure 3. GL-ErbB4$^+$ and GCL-ErbB4$^+$ neurons form inhibitory synapses onto MCs. ***A***, Representative traces showing light-induced inward current (top) and light-induced cell firing (bottom) in GL-ErbB4$^+$ neurons. ***B***, Representative traces showing light-induced inward current (top) and light-induced cell firing (bottom) in GCL-ErbB4$^+$ neurons. ***C***, Confocal images represent the morphology of a mitral cell, which has been recorded and backfilled with biocytin. Scale bar, 50 µm. ***D***, Representative traces showing light-induced PSCs in MCs (top), which could be blocked by BMI (bottom) but not by APV and CNQX (middle). ***E***, Representative traces showing the light-induced PSC in GL-ErbB4$^-$ neurons, which can be blocked by BMI but not APV and CNQX. ***F***, Representative traces showing the light-induced PSC in GCL-ErbB4$^-$ neurons, which can be blocked by BMI but not APV and CNQX. ***G***, Representative traces showing ErbB4$^-$ neurons, which have no response to optical stimulation.

suggesting that ErbB4$^+$ neurons form monosynaptic inputs onto MCs. Importantly, light-induced PSCs could not be blocked by AMPA and NMDA receptor antagonists CNQX (20 µM) and APV (50 µM), but by $GABA_A$ receptor antagonist BMI (20 µM) (Fig. 3*D*). These results suggest that ErbB4$^+$ neurons are GABAergic interneurons and provide monosynaptic inputs onto MCs. In addition to MCs, we also randomly recorded 30 ErbB4$^-$ neurons from layers other than ML. Fourteen of them (5 in GL, 2 in EPL, and 7 in GCL) responded to light stimulation with PSCs, but 16 (5 in GL, 3 in EPL, and 8 in GCL) did not (Fig. 3*E–G*). Light-induced PSCs in ErbB4$^-$ neurons could be blocked by $GABA_A$ receptor antagonist BMI (20 µM) but not CNQX (20 µM) and APV (50 µM) (Fig. 3*E*,*F*). These results suggest that GL- and GCL-ErbB4$^+$ neurons form direct inhibitory synapses onto MCs and many other neurons in the OB.

Distinct roles of GL- and GCL-ErbB4$^+$ neurons in regulating oscillations

To study the function of ErbB4$^+$ neurons, we explored the consequences of their activation on bulbar LFPs in free moving mice. Four tetrodes were arrayed semi-circularly around the lateral edge of the ferrule-bound optical fiber with glue, to produce a combined optical fiber-electrodes (Fig. 4*A*). The distance between the tips of the tetrodes and that of the optical fiber were adjusted based on which layers of ErbB4$^+$ cells to stimulate, aiming to keep the tips of tetrodes near the ML. To stimulate GCL-ErbB4$^+$ cells, the tip of optical fiber was 300-500 µm more dorsal than those of the tetrodes, whereas the tip of optical fiber was 300-500 µm more ventral to stimulate GL-ErbB4$^+$ neurons. The locations of the optical fibers were validated by postmortem histologic examination (Fig. 4*A*). Interestingly, stimulation of GCL-ErbB4$^+$ cells with 40 mW/mm^2 (10 s) light increased oscillations at theta (1-12 Hz) (pre vs light, $t_{(11)} = 3.92$, $p = 0.0024$; light vs post, $t_{(11)} = 4.12$, $p = 0.0017$, paired t test), β (12-30 Hz) (pre vs light, $t_{(11)} = 7.78$, $p < 0.001$; light vs post, $t_{(11)} = 8.2$, $p < 0.001$, paired t test), and low-γ (30-60 Hz) (pre vs light, $t_{(11)} = 6.34$, $p < 0.001$; light vs post, $t_{(11)} = 6.28$, $p < 0.001$, paired t test) frequencies but reduced the power of high-γ (60-100 Hz) (pre vs light, $t_{(11)} = 6.14$, $p < 0.001$; light vs post, $t_{(11)} = 7.53$, $p < 0.001$, paired t test) oscillation (Fig. 4*A–F*). These effects were reversible after the optical stimulation was stopped. These results suggest a role of ErbB4$^+$ neuron in OB oscillation.

We wondered that, at the intensity of 40 mW/mm^2, optical stimulation may activate ErbB4$^+$ neurons not only in GCL, but also those in other layers, whose activity may directly or indirectly contribute to oscillation. We reasoned that, if the stimulation is delivered at a minimal intensity, the effect should be GCL-ErbB4$^+$ neuron-specific. At 12 mW/mm^2, optical stimulation remained able to increase oscillation at theta (pre vs light, $t_{(11)} = 2.62$, $p = 0.024$; light vs post, $t_{(11)} = 2.36$, $p = 0.038$, paired t test), β (pre vs light, $t_{(11)} = 3.85$, $p = 0.0027$; light vs post, $t_{(11)} = 3.64$, $p = 0.0039$, paired t test), and low-γ (pre vs light, $t_{(11)} = 3.87$, $p = 0.0026$; light vs post, $t_{(11)} = 3.99$, $p = 0.0021$, paired t test) frequencies and reduce high-γ oscillation (pre vs light, $t_{(11)} = 2.79$, $p = 0.0177$; light vs post, $t_{(11)} = 2.75$, $p = 0.0189$, paired t test) (Fig. 4*G–L*). However, further reduction to 4 mW/mm^2 abolished light-induced changes in theta (pre vs light, $t_{(11)} = 0.5$, $p = 0.629$; light vs post, $t_{(11)} = 0.02$, $p = 0.984$, paired t test), β (pre vs light, $t_{(11)} = 0.24$, $p = 0.815$; light vs post, $t_{(11)} = 1.5$, $p = 0.162$, paired t test), and high-γ oscillations (pre vs light, $t_{(11)} = 0.4$, $p = 0.696$; light vs post, $t_{(11)} = 1.6$, $p = 0.139$, paired t test). Optical stimulation at 4 mW/mm^2 remained able to

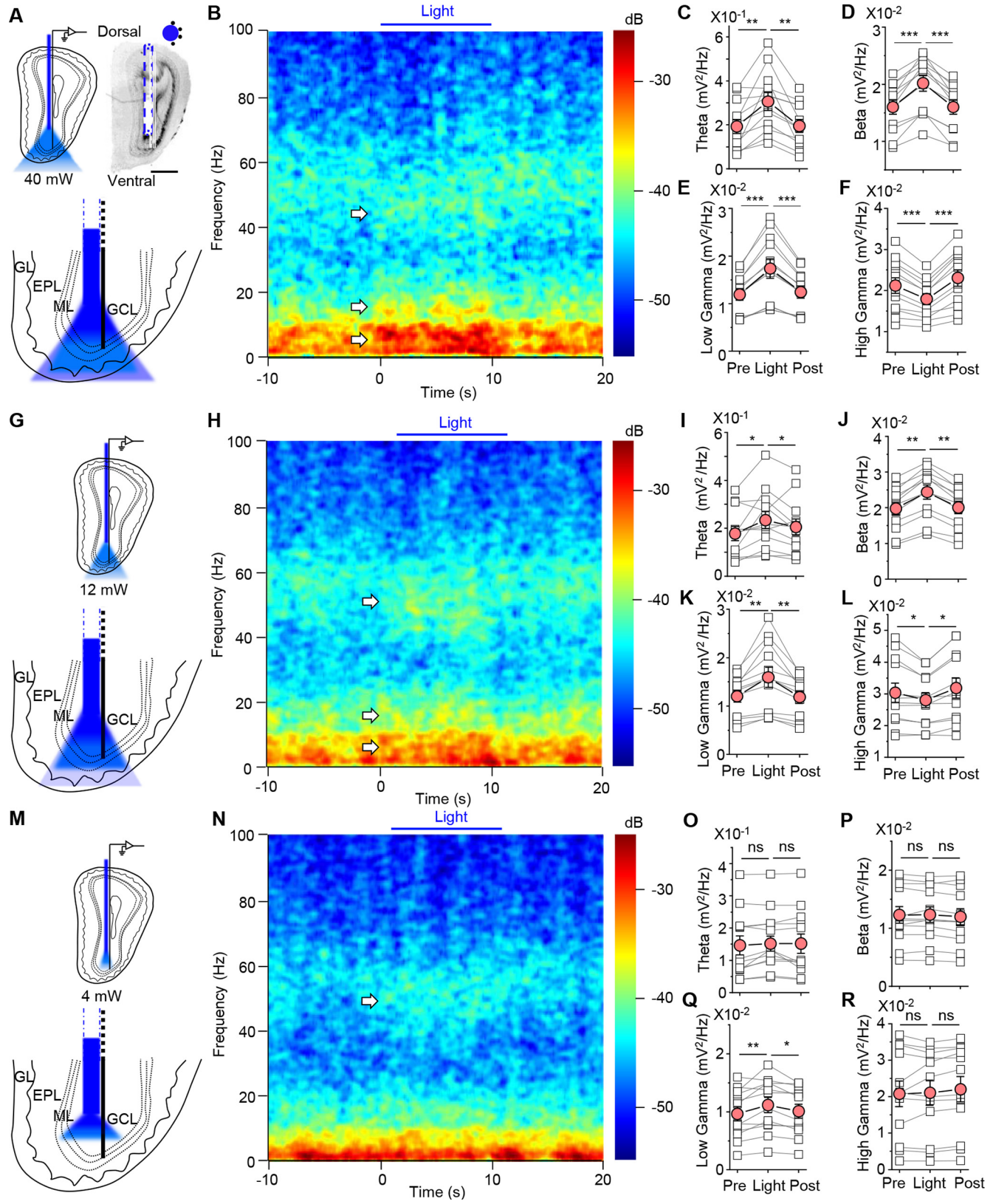

Figure 4. Optogenetic activation of GCL-ErbB4^{+} neurons increases low-γ oscillation. ***A***, Left, Schematic diagram of the OB showing the positions of the optic fiber and tetrodes, and the potential illuminating area by a high-power LED light (40 mW/mm^2) *in vivo*. Right, DIC image represents the position of optic fiber targeting GCL (outlined by dashed lines). White lines indicate tetrodes. Inset, Cross section of the optical fiber electrodes. Scale bar, 1 mm. ***B***, Representative power spectrum averaged from 5 trials showing the increased theta, β, and low-γ oscillations, and decreased high-γ oscillation during blue light stimulation (10 s, blue bar). ***C–F***, Summary of LFP powers in response to blue light stimulation in theta (***C***), β (***D***), low-γ (***E***), and high-γ (***F***) oscillations ($n = 12$ recordings from 3 mice). ***G***, Schematic diagram of the OB showing the position of the optic fiber and tetrodes, and the potential illuminating area by a medium-power LED light (12 mW/mm^2) *in vivo*. ***H***, Representative power spectrum averaged from 5 trials showing the increase of theta, β, and low-γ LFP power, and decrease of high-γ oscillation during blue light stimulation (10 s, blue bar). ***I-L***, Summary of LFP powers in response to blue light stimulation in theta (***I***), β (***J***), low-γ (***K***), and high-γ (***L***) oscillations ($n = 12$ recordings from 3

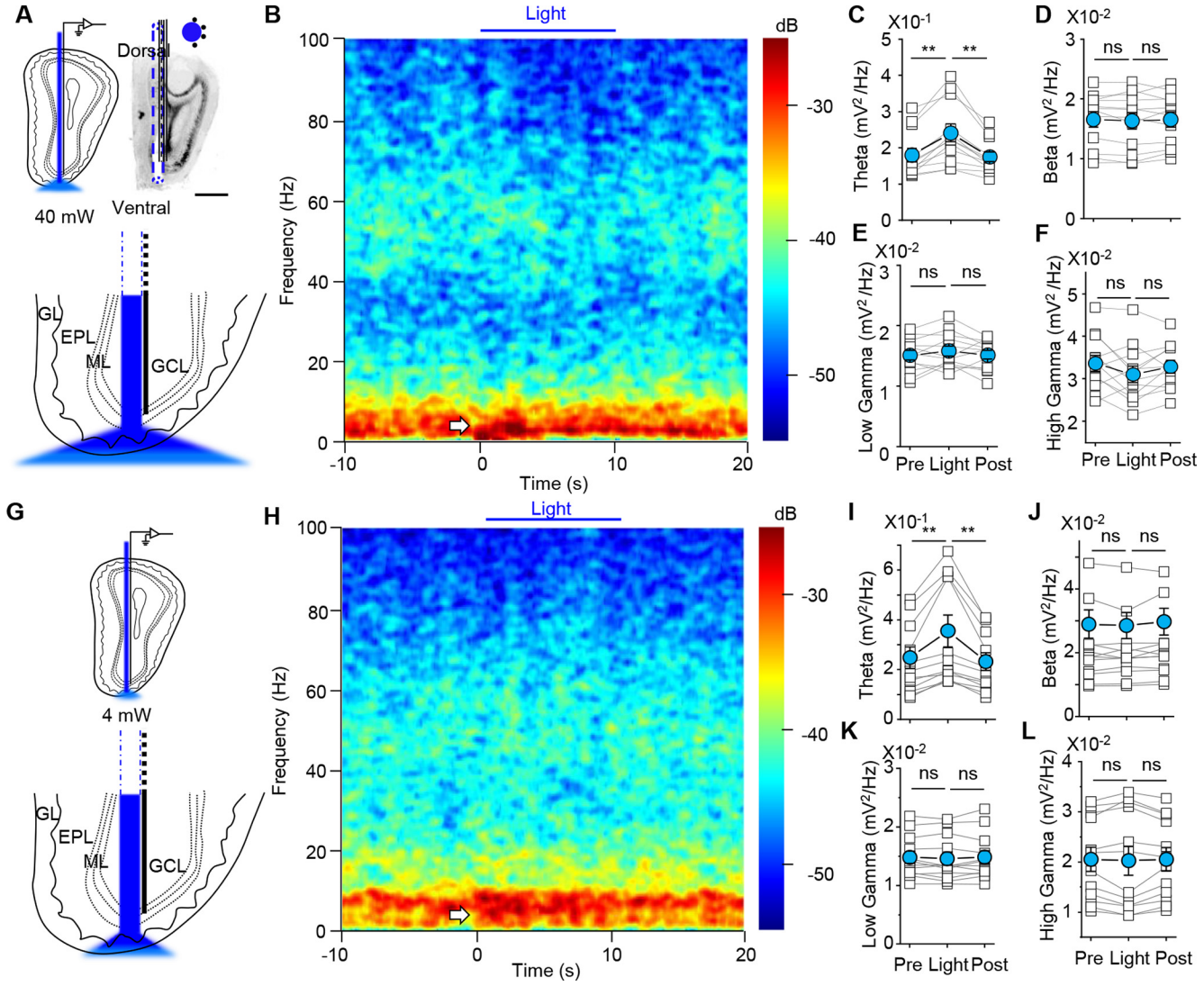

Figure 5. Optogenetic activation of GL-ErbB4$^+$ neurons increases theta oscillation. ***A***, Left, Schematic diagram of the OB represents the position of the optic fiber and tetrodes, and the potential illuminating area by a high-power LED light (40 mW/mm^2) *in vivo*. Right, DIC image represents the position of optic fiber targeting GL (outlined by dashed lines). Black lines indicate tetrodes. Inset, Cross section of the optical fiber electrodes. Scale bar, 1 mm. ***B***, Representative power spectrum averaged from 5 trials showing the increase of theta oscillation during blue light stimulation (10 s, blue bar). The increased theta oscillation is not sustained. ***C–F***, Summary of LFP powers in response to blue light stimulation in theta (***C***), β (***D***), low-γ (***E***), and high-γ (***F***) oscillations ($n = 12$ recordings from 3 mice). ***G***, Schematic diagram of the OB showing the position of the optic fiber and tetrodes, and the potential illuminating area by a low-power LED light (4 mW/mm^2) *in vivo*. ***H***, Representative power spectrum averaged from 5 trials showing the increase of theta oscillation during blue light stimulation (10 s, blue bar). ***I–L***, Summary of LFP powers in response to blue light stimulation in theta (***I***), β (***J***), low-γ (***K***), and high-γ (***L***) oscillations ($n = 12$ recordings from 3 mice). White arrow indicates changed bands. $^{**}p < 0.01$.

increase low-γ oscillation (pre vs light, $t_{(11)} = 3.2$, $p = 0.0084$; light vs post, $t_{(11)} = 3.65$, $p = 0.0038$, paired t test) (Fig. 4*M–R*). This intensity reduction-dependent effects suggest that GCL-ErbB4$^+$ neurons may specifically contribute to the generation of low-γ oscillation.

To stimulate GL-ErbB4$^+$ neurons, combined optical fiber-electrodes were implanted with the tip of optical fiber in the GL (Fig. 5*A*). Stimulation at 40 mW/mm^2 (10 s) induced a robust increase of theta (pre vs light, $t_{(11)} = 4.33$, $p = 0.0012$; light vs post, $t_{(11)} = 3.68$, $p = 0.0036$, paired t test) oscillation, which lasted ~4 s but had no significant changes in β (pre vs light, $t_{(11)} = 0.89$, $p = 0.391$; light vs post, $t_{(11)} = 0.57$, $p = 0.58$, paired t test), low (pre vs light, $t_{(11)} = 1.27$, $p = 0.229$; light vs post, $t_{(11)} = 1.04$, $p = 0.321$, paired t test), and high-γ (pre vs light, $t_{(11)} = 1.81$, $p = 0.098$; light vs post, $t_{(11)} = 1.69$, $p = 0.12$, paired t test) oscillations (Fig. 5*A–F*). This short-lasting increase of theta oscillation resembled the fatigue firing pattern of GL-ErbB4$^+$ neurons in response to strong current injection or light stimulation (Figs. 2*G*, 3*A*). To test this notion, we lowered the optical stimulation intensity to 4 mW/mm^2, which could induce continuous PG cell firing *in vitro* (data not shown). At this intensity, light stimulation caused a sustained increase of theta oscillation (pre vs light, $t_{(11)} = 3.37$, $p = 0.0063$; light vs post, $t_{(11)} = 3.89$, $p = 0.0025$, paired t test) (Fig. 5*G–L*). It is worthy pointing out that the 4 mW/mm^2 light stimulation had no effect on β (pre vs light, $t_{(11)} = 1.62$,

←

mice). ***M***, Schematic diagram of the OB showing the position of the optic fiber and tetrodes, and the potential illuminating area by a low-power LED light (4 mW/mm^2) *in vivo*. ***N***, Representative power spectrum averaged from 5 trials showing the increase of low-γ oscillation during blue light stimulation (10 s, blue bar). ***O–R***, Summary of LFP powers in response to blue light stimulation in theta (***O***), β (***P***), low-γ (***Q***), and high-γ (***R***) oscillations ($n = 12$ recordings from 3 mice). White arrow indicates changed bands. $^{*}p < 0.05$. $^{**}p < 0.01$. $^{***}p < 0.001$.

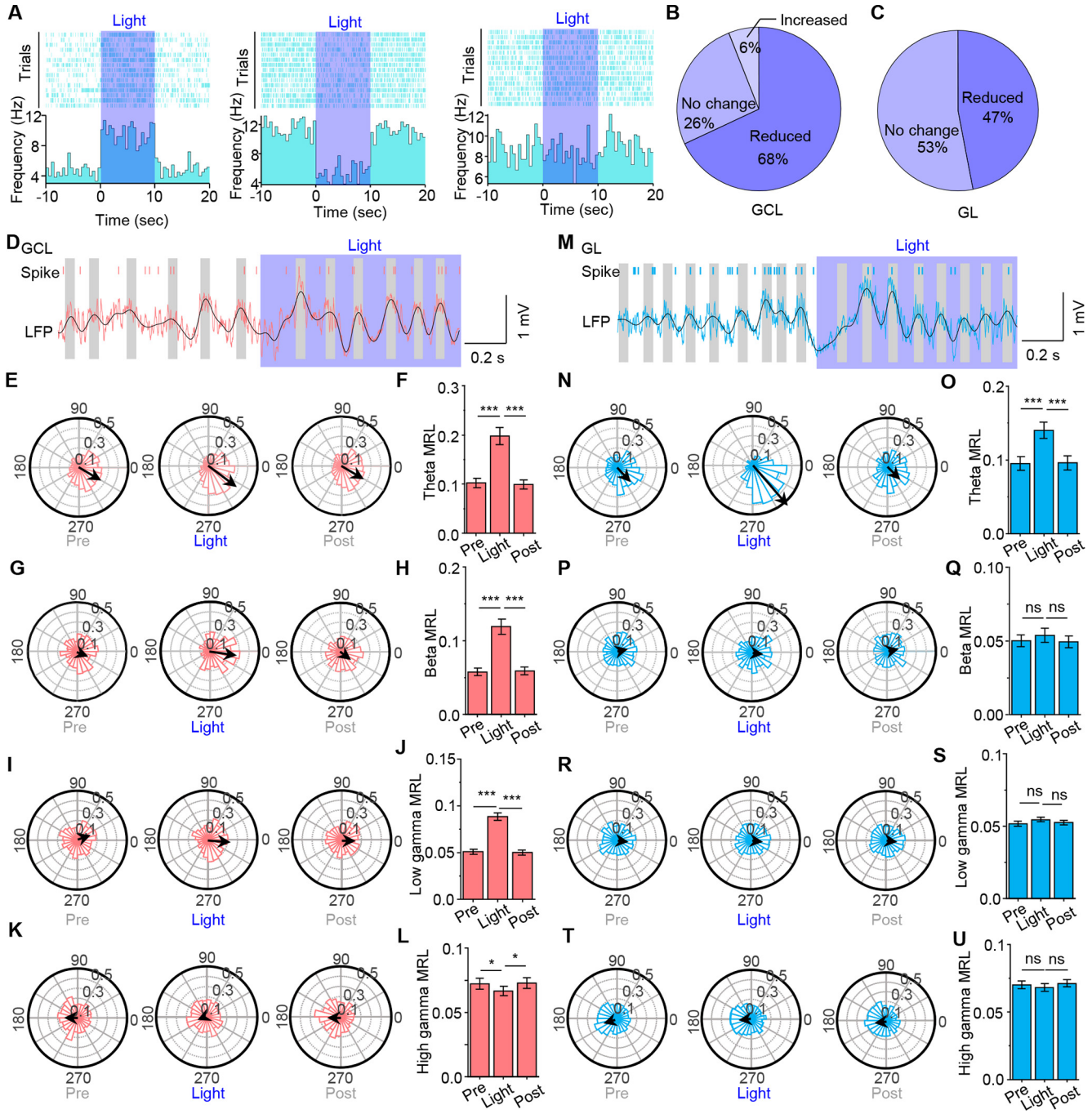

Figure 6. Optogenetic activation of ErbB4^{+} neurons increases local spike-phase locking. ***A***, Representative *in vivo* multiunit raster in *ErbB4-ChR2* mice showing the increase (left), decrease (middle), and no change (right) of firing rate in response to blue light stimulation. ***B***, Pie chart represents the percentage of units with increased, decreased, and no change firing rate when 40 mW/mm^2 light was delivered and optical fiber was in the GCL. (***C***) Pie chart represents the percentage of units with decreased and no change firing rate when 40 mW/mm^2 light was delivered and optical fiber was in the GL. ***D***, Examples of *in vivo* recording traces showing spikes recorded from a bulbar neuron (vertical lines) in relation to raw bulbar LFPs (red) and filtered theta oscillation (black) when optic fiber was placed in the GCL. ***E***, Example circular theta phase histogram of a single unit showing the preferred spike phase angle relative to the theta oscillation cycle before (left), during (middle), and after (right) 40 mW/mm^2 light stimulation. ***F***, Summary of the increased theta phase spike-phase locking in response to 40 mW/mm^2 light stimulus in the GCL ($n = 74$ units from 3 mice). ***G***, Example circular beta phase histogram of a single unit showing the preferred spike phase angle relative to the beta oscillation cycle before (left), during (middle), and after (right) 40 mW/mm^2 light stimulation. ***H***, Summary of the increased beta phase spike-phase locking in response to 40 mW/mm^2 light stimulus in the GCL ($n = 74$ units from 3 mice). ***I***, Example circular low-γ phase histogram of a single unit showing the preferred spike phase angle relative to the γ oscillation cycle before (left), during (middle), and after (right) 40 mW/mm^2 light stimulation. ***J***, Summary of the increased low-γ phase spike-phase locking in response to 40 mW/mm^2 light stimulus in the GCL ($n = 74$ units from 3 mice). ***K***, Example circular high-γ phase histogram of a single unit showing the preferred spike phase angle relative to the high-γ oscillation cycle before (left), during (middle), and after (right) 40 mW/mm^2 light stimulation. ***L***, Summary of the decreased high-γ phase spike-phase locking in response to 40 mW/mm^2 light stimulus in the GCL ($n = 74$ units from 3 mice). ***M***, Examples of *in vivo* recording traces showing spikes recorded from a bulbar neuron (vertical lines) in relation to raw bulbar LFPs (red) and filtered theta oscillation (black) when optic fiber was placed in GL layer. ***N***, Example circular theta phase histogram of a single unit showing the preferred spike phase angle relative to the theta oscillation cycle before (left), during (middle), and after (right) 40 mW/mm^2 light stimulation. ***O***, Summary of the increased theta phase spike-phase locking in response to 40 mW/mm^2 light stimulus in the GL ($n = 96$ units from 3 mice). ***P***, Example circular beta phase histogram of a single unit showing the preferred spike phase angle relative to the beta oscillation cycle before (left), during (middle), and after (right) 40 mW/mm^2 light stimulation. ***Q***, No change of summarized beta phase spike-phase locking in response to 40 mW/mm^2 light stimulus in the GL ($n = 96$ units from 3 mice). ***R***, Example circular low-γ phase histogram

$p = 0.134$; light vs post, $t_{(11)} = 1.24$, $p = 0.241$, paired t test), low-γ (pre vs light, $t_{(11)} = 0.96$, $p = 0.356$; light vs post, $t_{(11)} = 0.91$, $p = 0.38$, paired t test), and high-γ (pre vs light, $t_{(11)} = 0.85$, $p = 0.412$; light vs post, $t_{(11)} = 0.58$, $p = 0.571$, paired t test) oscillations (Fig. 5*G–L*). These data indicate that GL-ErbB4$^+$ neuron activation is likely involved in theta oscillation. Together, these observations suggest a role of GL-ErbB4$^+$ neurons in OB theta oscillation and GCL-ErbB4$^+$ neurons in low-γ oscillations.

Activation of ErbB4$^+$ neurons increases local spike-phase locking

To investigate how ErbB4$^+$ neurons influence the bulbar oscillations, we analyzed the light-induced unit activities in the OB. When optic fiber was placed in the GCL, firing rates were reduced in ~68% units, increased in ~6% units, and not changed in ~26% units (Fig. 6*A*,*B*). When optic fiber was placed in the GL, firing rates were reduced in ~47% units and not changed in ~53% units (Fig. 6*C*). No units were found with increased firing, probably because the recording electrodes were located in the ML, whereas the optical fiber tip was located in the GL (Fig. 5*A*), and dendrites of GL-ErbB4$^+$ neurons were restricted in the GL (Fig. 2*A*,*B*). Next, we determined whether neuronal spikes were phase-locked with LFPs at different frequencies before, during, and after light stimulation. The phase-locking intensity was measured by MRL, which is based on the average circular concentration of phase distribution (Sigurdsson et al., 2010). The MRL has a range from 0 to 1, with 1 as maximal phase synchronization of neuronal spikes with LFPs (Kato et al., 2013; Tan et al., 2018). As shown by the circular distribution of phase angles of spikes (20 degrees per bin size), the preferred phase angles were rarely changed by light stimulation of ErbB4$^+$ neurons. However, their distributions were more polarized in theta (pre vs light, $t_{(73)} = 9.1$, $p < 0.001$; light vs post, $t_{(73)} = 8.92$, $p < 0.001$, paired t test), β (pre vs light, $t_{(73)} = 9.57$, $p < 0.001$; light vs post, $t_{(73)} = 9.48$, $p < 0.001$, paired t test), and low-γ (pre vs light, $t_{(73)} = 7.57$, $p < 0.001$; light vs post, $t_{(73)} = 7.13$, $p < 0.001$, paired t test) oscillations, with increased MRL values (Fig. 6*D–J*). The phase distribution was less polarized in high-γ (pre vs light, $t_{(73)} = 2.24$, $p = 0.028$; light vs post, $t_{(73)} = 2.55$, $p = 0.013$, paired t test) oscillation with decreased MRL values (Fig. 6*K*,*L*). This change of spike phase-locking was reservable as it would drop to basal level once the stimulus stopped. On the other hand, when GL-ErbB4$^+$ neurons were activated, the circular distribution of the spike phase angles was more polarized in theta (pre vs light, $t_{(95)} = 5.74$, $p < 0.001$; light vs post, $t_{(95)} = 6.09$, $p < 0.001$, paired t test) oscillations but not in β (pre vs light, $t_{(95)} = 1.75$, $p = 0.083$; light vs post, $t_{(95)} = 1.93$, $p = 0.057$, paired t test), low-γ (pre vs light, $t_{(95)} = 1.41$, $p = 0.162$; light vs post, $t_{(95)} = 1.14$, $p = 0.259$, paired t test), or high-γ (pre vs light, $t_{(95)} = 0.85$, $p = 0.395$; light vs post, $t_{(95)} = 1.13$, $p = 0.26$, paired t test) oscillations (Fig. 6*M–U*). Together, these data support a model that the activation of bulbar ErbB4$^+$ neurons boosts local synchrony for bulbar oscillations.

NRG1 promotes GABA transmission in the OB

ErbB4 is a transmembrane tyrosine kinase that can be activated by NRG1 (Mei and Xiong, 2008; Mei and Nave, 2014). In the cortex and hippocampus, NRG1 promotes GABA release and thus regulates the activity of pyramidal neurons (Woo et al., 2007; Chen et al., 2010; Del Pino et al., 2013; Tan et al., 2018). To investigate whether the GABAergic transmission from ErbB4$^+$ interneurons to MCs is regulated by the NRG1-ErbB4 signaling, we isolated mIPSC from MCs by incubating OB slices in 10 μM CNQX, 50 μM APV, and 0.5 μM TTX. As shown in Figure 7*A–D*, 5 nM NRG1 increased mIPSC frequency (base vs NRG1, $t_{(6)} = 2.87$, $p = 0.014$; NRG1 vs wash, $t_{(6)} = 2.67$, $p = 0.037$, paired t test) but not amplitude (base vs NRG1, $t_{(6)} = 0.37$, $p = 0.721$; NRG1 vs wash, $t_{(6)} = 0.73$, $p = 0.493$, t test) within 5 min. This effect was reversible as it could be completely washed out. It was specific because NRG1 had little effects on the frequency or amplitude of mEPSC of MCs (frequency: base vs NRG1, $t_{(6)} = 0.28$, $p = 0.787$; NRG1 vs wash, $t_{(6)} = 0.34$, $p = 0.749$. amplitude: base vs NRG1, $t_{(6)} = 0.38$, $p = 0.717$; NRG1 vs wash, $t_{(6)} = 0.25$, $p = 0.809$, paired t test) (Fig. 7*E–G*). We also recorded eIPSC by placing a concentric electrode in the GCL in the presence of 10 μM CNQX and 50 μM APV. The eIPSC amplitudes were increased by NRG1 (base vs NRG1, $t_{(5)} = 2.89$, $p = 0.034$; NRG1 vs wash, $t_{(5)} = 5.03$, $p = 0.004$, paired t test) (Fig. 7*H*,*I*). These studies indicated a role of the NRG1 signaling in promoting the GABA transmission from ErbB4$^+$ neurons onto MCs. To reveal the underlying mechanisms, we examined the paired-pulse ratio (PPR) of eIPSCs. NRG1 reduced the PPRs at various interpulse intervals (25 ms, $t_{(11)} = 2.96$, $p = 0.013$; 50 ms, $t_{(11)} = 2.53$, $p = 0.028$; 100 ms, $t_{(11)} = 2.44$, $p = 0.033$; 200 ms, $t_{(11)} = 2.59$, $p = 0.025$; and 500 ms $t_{(11)} = 3.31$, $p = 0.007$, paired t test) (Fig. 7*J*,*K*), suggesting that NRG1 acts by increasing the probability of presynaptic GABA release. To determine whether NRG1 alters the intrinsic excitability of GL-ErbB4$^+$ and GCL-ErbB4$^+$ neurons, we examined neuron firing in response to injected step currents (−25 pA to 200 pA at 25 pA per step) in the presence of APV (50 μM), CNQX (20 μM), and BMI (10 μM). NRG1 had no significant impact on neuronal excitability (GL-ErbB4$^+$ neuron: $F_{(9,120)} = 0.02$, $p = 0.875$; GCL-ErbB4$^+$ neuron: $F_{(9,120)} = 0.6$, $p = 0.441$, ANOVA) (Fig. 7*L–O*). These results suggest that NRG1 promotes GABA release through increasing releasing probability in the OB.

Impaired olfaction and attenuated LFP powers in ErbB4 mutant mice

First, we examined the effects of *Erbb4* mutation on GABAergic transmission. ErbB4 null mutant mice die prematurely because of cardiac deficits (Tidcombe et al., 2003). To prevent embryonic lethality, *ErbB4-null* mice were crossed with α-myosin heavy chain *(αMHC)-ErbB4* transgenic mice, and resulting *ErbB4-null; aMHC-ErbB4* mice (hereafter referred to as *ErbB4*$^{-/-}$) are able to survive for >1 year (Tidcombe et al., 2003). We recorded mIPSCs and mEPSCs in MCs. As shown in Figure 8*A–C*, mIPSC frequency ($t_{(12)} = 3.59$, $p = 0.0037$, t test), but not amplitude ($t_{(12)} = 0.4$, $p = 0.699$, t test), was reduced in *ErbB4*$^{-/-}$ OB slices, compared with those from control littermates (i.e., *αMHC-ErbB4* transgenic mice), suggesting that GABAergic transmission requires ErbB4. PPRs of eIPSCs were increased in *ErbB4*$^{-/-}$ mice compared with control littermates (25 ms, $t_{(10)} = 0.42$, $p = 0.684$; 50 ms, $t_{(10)} = 0.74$, $p = 0.477$; 100 ms, $t_{(10)} = 2.59$,

←

of a single unit showing the preferred spike phase angle relative to the γ oscillation cycle before (left), during (middle), and after (right) 40 mW/mm^2 light stimulation. ***S***, No change of summarized low-γ spike-phase locking in response to 40 mW/mm^2 light stimulus in the GL ($n = 96$ units from 3 mice). ***T***, Example circular high-γ phase histogram of a single unit showing the preferred spike phase angle relative to the γ oscillation cycle before (left), during (middle), and after (right) 40 mW/mm^2 light stimulation. ***U***, No change of summarized high-γ spike-phase locking in response to 40 mW/mm^2 light stimulus in the GL ($n = 96$ units from 3 mice). For all the circular histogram, the arrow direction indicates preferred phase angle, and the arrow length indicates MRL value. *$p < 0.05$. ***$p < 0.001$.

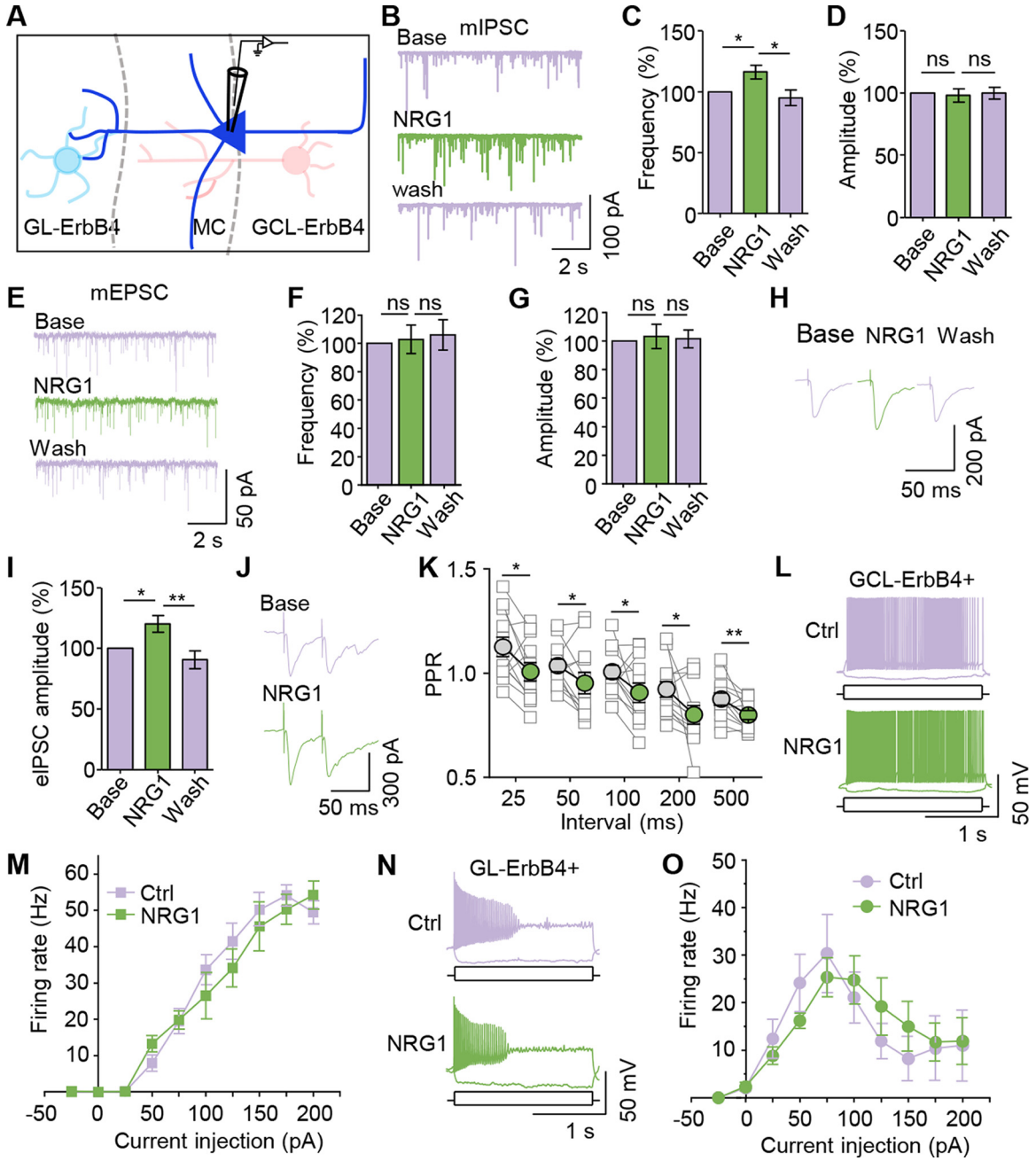

Figure 7. Promotion of GABA transmission onto MCs by NRG1. ***A***, Schematic diagram showing the slice recording paradigm of MCs. ***B***, Representative traces of mitral cell mIPSC recorded before, during, and after NRG1 application. ***C***, ***D***, Summary of mIPSC frequency (***C***) and amplitude (***D***) before, during, and after NRG1 application ($n = 7$ cells from 3 mice). ***E***, Representative traces of mitral cell mEPSC recorded before, during, and after NRG1 application. ***F***, ***G***, Summary of mEPSC frequency (***B***) and amplitude (***C***) before, during, and after NRG1 application ($n = 7$ cells from 3 mice). ***H***, Representative traces of mitral cell eIPSC before, during, and after NRG1 application. ***I***, Summary of mitral cell eIPSC showing the increased amplitude after NRG1 application, which can be washed out ($n = 6$ cells from 3 mice). ***J***, Representative traces of paired-pulse (interval, 50 ms) stimuli before and during NRG1 application. ***K***, Summarized data showing the decreased mitral cell eIPSC PPR by NRG1 ($n = 12$ neurons from 4 mice; paired t test). ***L***, Representative traces of GCL-ErbB4$^+$ neurons in responding to step current injection in the presence of NRG1. ***M***, Input–output curve showing the excitability of GCL-ErbB4$^+$ neurons in the presence of NRG1 ($n = 7$ cells from 3 mice). ***N***, Representative traces of GL-ErbB4$^+$ neurons in responding to step current injection in the presence of NRG1. ***O***, Input–output curve showing the excitability of GL- ErbB4$^+$ neurons in the presence of NRG1 ($n = 7$ cells from 3 mice). $^*p < 0.05$. $^{**}p < 0.01$.

$p = 0.027$; 200 ms, $t_{(10)} = 2.83$, $p = 0.018$; and 500 ms $t_{(10)} = 2.39$, $p = 0.038$, t test) (Fig. 8*D*,*E*). However, both frequency ($t_{(14)} = 0.26$, $p = 0.795$, t test) and amplitude ($t_{(14)} = 0.63$, $p = 0.537$, t test) of mEPSCs were similar between the two genotypes (Fig. 8*F*–*H*). These data suggest that the inhibitory but not excitatory synaptic transmission was diminished in the OB of *ErbB4*$^{-/-}$ mice.

Next, we recorded LFPs in the OB in free moving mice through implanted tetrodes (Fig. 8*I*,*J*). The power of bulbar LFP correlates with exploring behavior and the task demand (Martin et al., 2006; Kay et al., 2009; Lepousez and Lledo, 2013; Martin and Ravel, 2014). Therefore, we focused on the power while mice were running at speeds >2 cm/s, to minimize the variation of data (Sigurdsson et al., 2010). As shown in Figure 8*K*–*M*, the bulbar LFP power was reduced at theta ($t_{(25)} = 5.5$, $p < 0.001$, t test), β ($t_{(25)} = 3.69$, $p = 0.001$, t test), and γ ($t_{(25)} = 2.83$, $p = 0.009$, t test) oscillations in *ErbB4*$^{-/-}$ mice, compared with control mice.

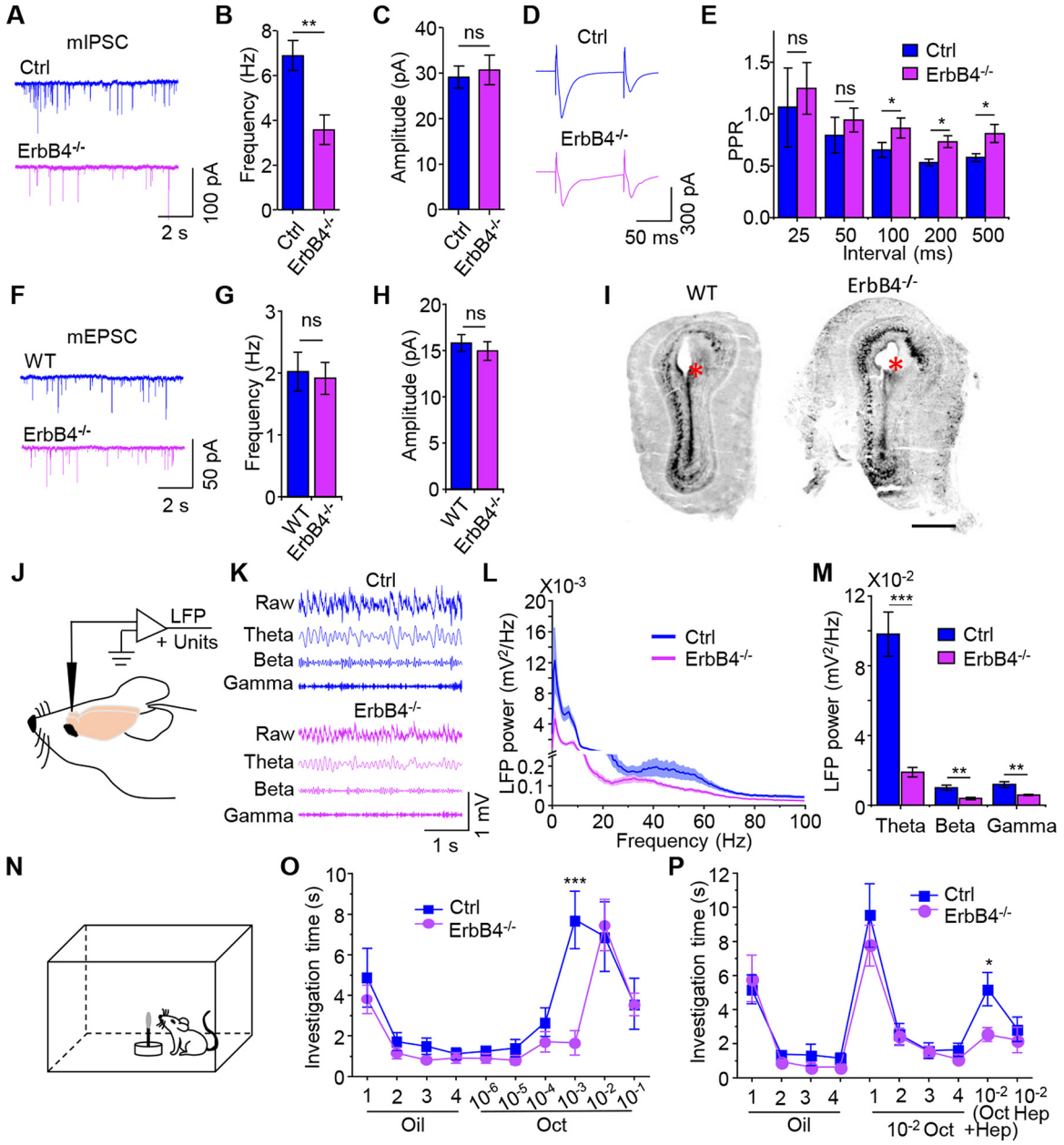

Figure 8. Reduced bulbar LFP power and impaired olfaction in *ErbB4*$^{-/-}$ mice. ***A***, Representative traces of mitral cell mIPSCs recorded from bulbar slices of control and *ErbB4*$^{-/-}$ mice. ***B***, ***C***, Summary of mitral cell mIPSC frequency (***B***) and amplitude (***C***) in control and *ErbB4*$^{-/-}$ mice ($n = 7$ cells from 3 mice for each group). ***D***, Representative traces of paired-pulse (interval, 0.1 s) stimuli in control and *ErbB4*$^{-/-}$ mice. ***E***, Summarized data showing the increased mitral cell eIPSC PPR in *ErbB4*$^{-/-}$ compared with control littermate (control, $n = 6$ cells from 3 mice; *ErbB4* $^{-/-}$, $n = 8$ cells from 4 mice). ***F***, Representative traces of mitral cell mEPSC from control and *ErbB4*$^{-/-}$ mice. ***G***, ***H***, Summary of mitral cell mEPSC frequency (***G***) and amplitude (***H***) in control and *ErbB4*$^{-/-}$ mice ($n = 8$ cells from 3 mice for each group). ***I***, DIC image represents the electrode positions, which have lesions made by electronic heat (red star). Scale bar, 1 mm. ***J***, Schematic diagram of *in vivo* free-moving mice electrophysiological recording from the OB. ***K***, Representative traces of LFP signals from the OB of control and *ErbB4*$^{-/-}$ mice. Raw LFP signals were band filtered to isolate theta, β, and γ oscillations, respectively. ***L***, Bulbar LFP powers showing in whole spectrum in control and *ErbB4*$^{-/-}$ mice (control $n = 15$ recordings, 3 mice; *ErbB4*$^{-/-}$ $n = 12$ recordings, 3 mice; two-way ANOVA, $F_{(204,5304)} = 12.28$, ***$p < 0.001$; *post hoc*, Bonferroni; theta, ***$p < 0.001$; β, ***$p < 0.01$; γ, **$p < 0.01$). ***M***, Summary of bulbar LFP powers. LFP powers in each oscillation were summed up for comparation (control, $n = 15$ recordings from 3 mice; *ErbB4*$^{-/-}$, $n = 12$ recordings from 3 mice). ***N***, Schematic diagram of the odor habituation–dishabituation behavioral testing. ***O***, Impaired olfactory sensitivity in *ErbB4*$^{-/-}$ mice compared with control mice (control, $n = 10$ mice; *ErbB4*$^{-/-}$, $n = 11$ mice). ***P***, Impaired odor discrimination of a pair of close odorants (octanal and heptanal) in *ErbB4*$^{-/-}$ mice compared with control mice ($n = 10$ mice for both group). *$p < 0.05$. **$p < 0.01$. ***$p < 0.001$.

These data suggest that the NRG1-ErbB4 signaling may play a role in regulating bulbar oscillations, which is critical for olfaction.

Finally, we determined whether ErbB4 mutation alters olfaction by measuring olfactory sensitivity and odor discrimination. *ErbB4*$^{-/-}$ mice were sequentially presented for 2 min with swab-carried mineral oil (4 times) followed by increasing concentrations of octanal (10^{-6} to 10^{-1} in mineral oil with the increasement of 10) (Fig. 8*N*) and monitored for sniffing or investigation time. As shown in Figure 8*O*, the sensory threshold of control mice was at 10^{-3} dilution; in contrast, the curve was shifted to the right for *ErbB4*$^{-/-}$ mice, with a threshold at 10^{-2} dilution, suggesting that olfactory sensitivity is impaired in *ErbB4*$^{-/-}$ mice ($t_{(19)} = 3.93$, $p < 0.001$, *t* test). Next, we performed the odor discrimination test by presenting the mice with octanal at 10^{-2} dilution for 4 times, followed by a mixture

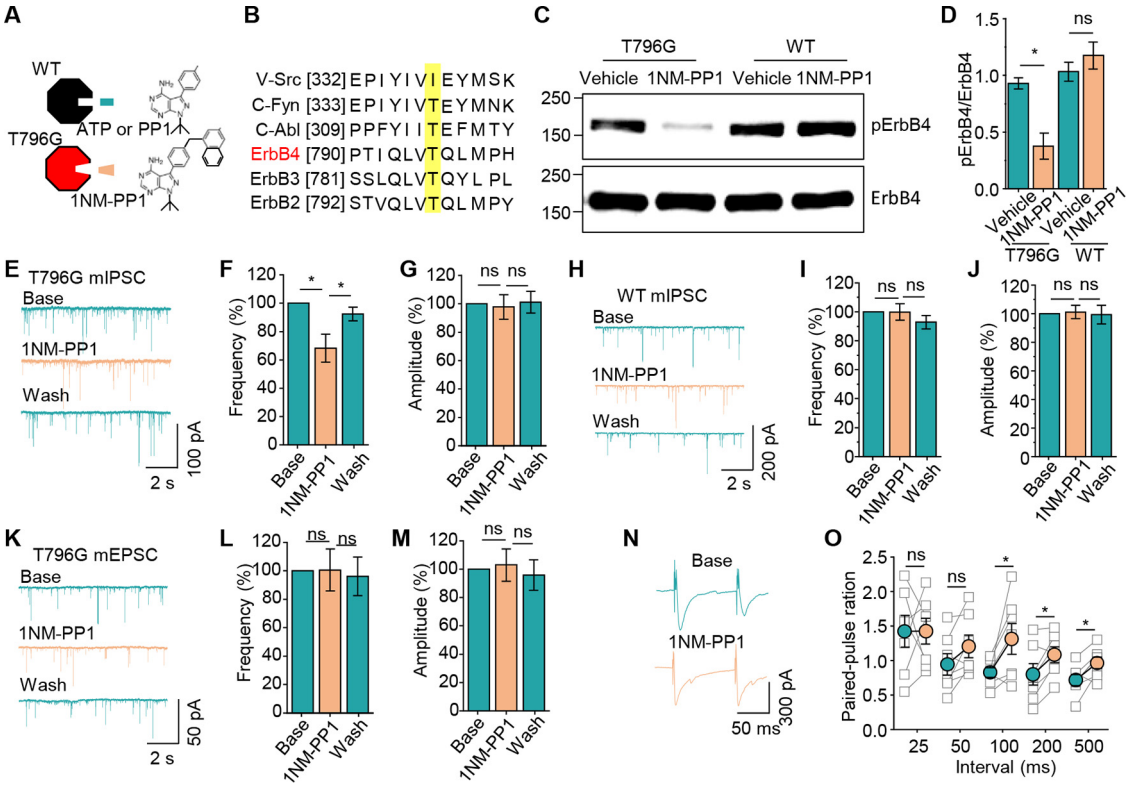

Figure 9. Reduced GABAergic transmission, bulbar oscillation, and olfaction by chemical genetic inhibition of ErbB4. ***A***, Diagram of the chemical-sensitive mutant protein kinases and structures of PP1 and its analog 1NM-PP1. ***B***, Alignment of the amino acid sequence of various tyrosine kinase. Threonine (T) is a conserved residue. ***C***, ***D***, Inhibition of 1NM-PP1 on endogenous ErbB4 phosphorylation in *T796G* mice and control littermates ($n = 3$ samples for both groups). ***E***, Representative traces of mitral cell mIPSC before, during, and after 1NM-PP1 application. ***F***, ***G***, Summary of mIPSC frequency (***F***) and amplitude (***G***) before, during, and after 1NM-PP1 application ($n = 7$ cells from 4 mice). ***H***, Representative traces of mitral cell mIPSC recorded before, during, and after 1NM-PP1 application in WT mice. ***I***, ***J***, Summary of mEPSC frequency (***I***, $n = 9$ cells from 4 mice) and amplitude (***J***, $n = 9$ cells from 4 mice) before, during, and after 1NM-PP1 application. ***K***, Representative traces of mitral cell mEPSC recorded before, during, and after 1NM-PP1 application in *T796G* mice. ***L***, ***M***, Summary of mEPSC frequency (***L***, $n = 7$ cells from 4 mice) and amplitude (***M***, $n = 7$ cells from 4 mice) before, during, and after 1NM-PP1 application. ***N***, Representative traces of paired-pulse (interval, 0.1 s) stimuli before and during 1NM-PP1 application. ***O***, Increased mitral cell eIPSC PPR by 1NM-PP1 ($n = 7$ cells from 3 mice). $^*p < 0.05$.

of 10^{-2} octanal and 10^{-2} heptanal, two structurally close odors (Fig. 8*P*). Control mice showed increased sniffing time when the mixture of octanal and heptanal was presented, indicating the ability to recognize the new odor. However, the increase in sniffing time was less in *ErbB4*$^{-/-}$ mice, indicative of impaired ability to discriminate odorants ($t_{(18)} = 2.53$, $p = 0.021$, *t* test). Together, these observations support a model that the NRG1-ErbB4 signaling is key to olfaction by regulating GABAergic transmission and local oscillation in the OB.

Dynamic OB ErbB4 kinase activity for GABAergic transmission, oscillation, and olfaction

ErbB4 regulates adult neurogenesis in the OB (Anton et al., 2004), which may complicate the interpretation of data from studying *ErbB4*$^{-/-}$ mice. To investigate whether the kinase activity of ErbB4 regulates olfaction, we took a chemical genetic strategy (Bishop et al., 2000) to enlarge the ATP binding pocket of ErbB4 by mutating threonine 796 to glycine (Tan et al., 2018) (Fig. 9*A*,*B*). The *T796G* mutation enables specific inhibition of ErbB4 by the bulky inhibitor 1NM-PP1. *T796G* knockin mice have served as an informative model to reveal the function of ErbB4 kinase activity in the hippocampus and cortex (Tan et al., 2018). Remarkably, 1NM-PP1 injection into the OB (50 μM, 0.5 μl) reduced phosphorylated ErbB4 in the OB in *T796G* mice ($t_{(4)} = 4.48$, $p = 0.011$, *t* test), but not in control mice ($t_{(4)} = 0.98$, $p = 0.384$, *t* test) (Fig. 9*C*,*D*). In accord, 1NM-PP1 reduced the frequency (base vs 1NM-PP1, $t_{(6)} = 3.23$, $p = 0.018$; 1NM-PP1 vs wash, $t_{(6)} = 3.18$, $p = 0.019$, paired *t* test) but not amplitude (base vs 1NM-PP1, $t_{(6)} = 0.26$, $p = 0.806$; 1NM-PP1 vs wash, $t_{(6)} = 0.35$, $p = 0.74$, paired *t* test) of mIPSCs in *T796G* OB slices (Fig. 9*E*–*G*). The same concentration of 1NM-PP1 had little effect on both the frequency (base vs 1NM-PP1, $t_{(8)} = 0.03$, $p = 0.973$; 1NM-PP1 vs wash, $t_{(8)} = 1.27$, $p = 0.24$, paired *t* test) and amplitude (base vs 1NM-PP1, $t_{(8)} = 0.26$, $p = 0.804$; 1NM-PP1 vs wash, $t_{(8)} = 0.39$, $p = 0.706$, paired *t* test) of mIPSCs of OB slices from control mice (Fig. 9*H*–*J*). In addition, 1NM-PP1 had no effect on the frequency (base vs 1NM-PP1, $t_{(6)} = 0.05$, $p = 0.965$; 1NM-PP1 vs wash, $t_{(6)} = 0.4$, $p = 0.706$, paired *t* test) and amplitude (base vs 1NM-PP1, $t_{(6)} = 0.26$, $p = 0.806$; 1NM-PP1 vs wash, $t_{(6)} = 2.36$, $p = 0.056$, paired *t* test) of mEPSCs (Fig. 9*K*–*M*). These data demonstrate that acute inhibition of ErbB4 specifically reduces GABAergic transmission in the OB. Mechanistically, 1NM-PP1 increased the PPR of eIPSCs (25 ms, $t_{(6)} = 0.01$, $p = 0.991$; 50 ms, $t_{(6)} = 2.29$, $p = 0.062$; 100 ms, $t_{(6)} = 2.59$, $p = 0.041$; 200 ms, $t_{(6)} = 3.07$, $p = 0.022$; and 500 ms $t_{(6)} = 3.07$, $p = 0.022$, paired *t* test) (Fig. 9*N*,*O*), suggesting decreased GABA release probability.

Next, we examined the effect of acute inhibition of ErbB4 on bulbar oscillations by implanting a cannula and tetrode in the OB of *T796G* mice (Fig. 10*A*–*C*). The cannula was placed on the top of OB to ensure the drug spread the entire OB and minimize recording interference. 1NM-PP1 (50 μM, 0.5 μl) or the same volume of vehicle was delivered to the OB. As described above, LFP power was only analyzed when mice were exploring at speeds faster than 2 cm/s. As shown in Figure 10*D*, *E*, the bulbar

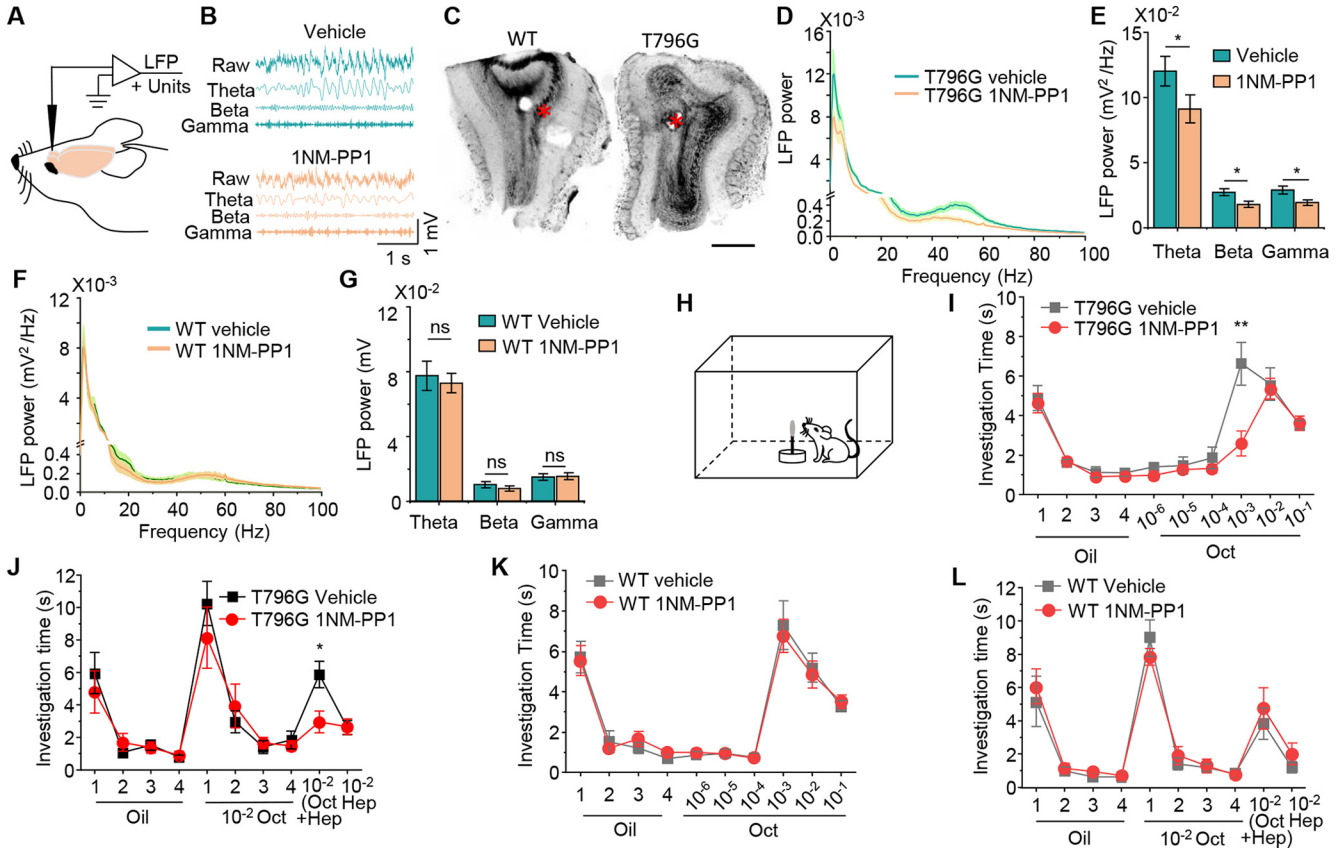

Figure 10. Chemical genetic inhibition of ErbB4 reduces LFP power and impair olfaction. ***A***, Schematic diagram of *in vivo* free-moving mice electrophysiological recording from the OB. ***B***, Representative traces of LFP signals from the OB after the local injection of vehicle or 1NM-PP1. Raw LFP signals were band filtered to isolate theta, β, and γ oscillations, respectively. ***C***, DIC image represents the electrode positions, which have lesions made by electronic heat (red star). Scale bar, 1 mm. ***D***, Bulbar LFP powers showing in whole spectrum after the local injection of vehicle or 1NM-PP1 ($n = 16$ recordings from 3 mice for both vehicle and 1NM-PP1 injection; two-way ANOVA, $F_{(204,6324)} = 19.91$, $^{***}p < 0.001$; *post hoc*, Bonferroni; theta, $^{**}p < 0.01$; β, $^{**}p < 0.01$; γ, $^{***}p < 0.01$). ***E***, Bulbar LFP powers showing in columns. LFP powers in each oscillation were summed up for comparation ($n = 16$, *t* test, $^{*}p < 0.05$). ***F***, Bulbar LFP powers showing in whole spectrum after the local injection of vehicle or 1NM-PP1 in WT mice ($n = 13$ recordings from 3 mice for both vehicle and 1NM-PP1 injection; two-way ANOVA, $F_{(204,5100)} = 0.428$, not significant, $p = 0.569$). ***G***, Bulbar LFP powers showing in columns. LFP powers in each oscillation were summed up for comparation ($n = 13$ recordings from 3 mice). ***H***, Schematic diagram of the odor habituation–dishabituation behavioral testing. ***I***, Impaired olfactory sensitivity in *T796G* mice after local injection of 1NM-PP1 compared with vehicle ($n = 10$ mice for both groups). ***J***, Impaired odor discrimination of a pair of close odorants (octanal and heptanal) in *T796G* mice after local injection of 1NM-PP1 compared with vehicle (vehicle, $n = 13$ mice; 1NM-PP1, $n = 12$ mice). ***K***, Little effect on olfactory sensitivity in WT mice after local injection of 1NM-PP1 compared with vehicle injection (vehicle, $n = 12$ mice; 1NM-PP1 $n = 13$ mice). ***L***, Little effect on odor discrimination of a pair of close odorants (octanal and heptanal) in WT mice after local injection of 1NM-PP1 compared with vehicle injection (vehicle, $n = 9$ mice; 1NM-PP1, $n = 10$ mice).

LFP power was reduced at theta ($t_{(30)} = 2.18$, $p = 0.037$, *t* test), β ($t_{(30)} = 2.67$, $p = 0.012$, *t* test), and γ ($t_{(30)} = 2.61$, $p = 0.014$, *t* test) oscillations by 1NM-PP1, compared with those injected with the vehicle. 1NM-PP1 had no effect on LFP powers of WT mice (theta, $t_{(24)} = 0.42$, $p = 0.675$; β, $t_{(24)} = 0.91$, $p = 0.373$; γ, $t_{(24)} = 0.17$, $p = 0.867$, *t* test) (Fig. 10*F*,*G*). These results demonstrate that ErbB4 kinase activity is acutely required for normal bulbar oscillations. In accord, the threshold of *T796G* mice to sense octanal was increased with a rightward shift of the curve in the 1NM-PP1 local injection group compared with vehicle local injection group ($t_{(18)} = 3.2$, $p = 0.005$, *t* test) (Fig. 10*H*,*I*), indicating impaired odor sensitivity by ErbB4 inhibition. The ability of *T796G* mice to discriminate odorants was impaired in *T796G* mice after local 1NM-PP1 injection ($t_{(23)} = 2.77$, $p = 0.011$, *t* test) (Fig. 10*J*). 1NM-PP1 had no effect on odor sensation or odor discrimination in control mice (sensation: $t_{(23)} = 0.38$, $p = 0.71$; discrimination: $t_{(23)} = 0.57$, $p = 0.571$, *t* test) (Fig. 10*K*,*L*). These results indicate that the dynamic activity of ErbB4 is necessary for OB oscillation and normal olfaction. Together, these observations suggest that the NRG1-ErbB4 signaling in the OB is critical to olfaction by promoting GABAergic transmission and oscillation.

Discussion

Bulbar interneurons are heterogeneous in morphology, molecular marker expression, and electrophysiological property (Toida et al., 1998; Lledo et al., 2008; Nagayama et al., 2014). Here we identified ErbB4^{+} cells in the OB as a novel type of interneurons. They seldomly coexpress previously characterized interneuron markers in the OB and bear a distinct distribution pattern (Toida et al., 1998; Kiyokage et al., 2010; Kato et al., 2013). Functionally, they regulate bulbar oscillation and olfaction and enable the regulation by the NRG1-ErbB4 signaling. NRG1 is widely expressed in the brain. In the cortex and hippocampus, it is expressed in excitatory neurons, less in GABAergic neurons or astrocytes (X. Liu et al., 2011). In the OB, NRG1 was detected in ensheathing cells (Pollock et al., 1999), although it may be expressed in other types of cells (Ghashghaei et al., 2006; Wang et al., 2021).

Based on the location and morphology, bulbar interneurons can be classified into PG cells in the GL, GCs in the GCL, and SA

cells across all layers. PG cells in the GL have short dendrites that are generally thought to ramify in a single glomerulus (Pinching and Powell, 1971; Lledo et al., 2008; Nagayama et al., 2014). ErbB4$^+$ neurons in the GL are likely a subtype of PG cells because they are GABAergic and have short dendrites (Fig. 2*A*, *B*). PG cells can be further divided into two subtypes: Type I PG cells receive direct inputs from OSNs, and Type II PG cells are innervated by external tufted cells but not OSNs. Tufted cells are glutamatergic neurons that generate spontaneous bursts of APs (Imai, 2014; Nagayama et al., 2014). We found the latencies of eEPSC of GL-ErbB4$^+$ neurons (in response to stimulation of OSNs) clearly showed two groups (Fig. 2*E*,*F*). In addition, some GL-ErbB4$^+$ neurons generate bursts of sEPSCs while others produce relatively even sEPSC (data not shown). All this evidence proves that GL-ErbB4$^+$ neurons could be both Type I and Type II PG cells.

Most GCs are localized in the GCL, but some are found in the IPL and the ML (Nagayama et al., 2014). ErbB4$^+$ neurons are also located in the IPL/ML, with morphology and electrophysiological properties characteristic of GCs (Fig. 2*I*,*J*). Because GCs are axonless, their output relies on the reciprocal synapses with the secondary dendrites of MCs in the EPL (Yokoi et al., 1995; Isaacson and Strowbridge, 1998). Based on morphology, GCs can be separated into three morphologically distinct subgroups: Type I GCs send spiny dendrites throughout the EPL; Type II GCs extend dendrites only in the deep EPL; and Type III GCs ramify spiny dendrites predominantly in the superficial EPL (Yokoi et al., 1995; Isaacson and Strowbridge, 1998; Nagayama et al., 2014). GCL-ErbB4$^+$ neurons displayed morphologies of all three types (Fig. 2*I*,*J*). Deep short-axon cells are another type of interneurons in the GCL whose axons project to different layers of the OB, although their dendrites do not extend beyond the ML (Nagayama et al., 2014). Unlike deep short-axon cells, GCL-ErbB4$^+$ cells are axonless and extend dendrites to EPL.

Interneurons in the OB can also be classified based on molecular markers they express, such as TH, CB, CR, and PV. PG cells are molecularly heterogeneous, and GCs are molecularly less diverse (Kosaka and Kosaka, 2007; Kiyokage et al., 2010; Nagayama et al., 2014). TH$^+$ PG neurons that receive direct OSN inputs represent Type I PG neurons, while CB$^+$ PG cells with almost no OSN inputs are Type II PG (Kosaka and Kosaka, 2007). ErbB4$^+$ is expressed in both Type I and Type II PGs. Conversely, PV$^+$ neurons are mainly sited in the EPL, and CR$^+$ neurons are widely distributed across all layers (Toida et al., 1998; Kato et al., 2013). ErbB4 is partially colocalized with CB and is rarely colocalized with TH, CR, and PV. Therefore, ErbB4$^+$ neurons represent novel molecularly identified PGs and GCs in the OB.

Bulbar oscillations are key to olfaction. Odor processing is associated with β and γ oscillations in both insects and mammals (Martin and Ravel, 2014). Even in the absence of odor stimulation, γ bursts occur in animals that are freely exploring the environment (Kay et al., 2009; Lepousez and Lledo, 2013). However, how bulbar oscillations are generated is not fully understood. By using optogenetics, we found that activation of GL-ErbB4$^+$ neurons enhances theta oscillation, whereas activation of GCL-ErbB4$^+$ neurons increases γ oscillation, consistent with an earlier report (Fukunaga et al., 2014). γ oscillation could be further divided into low- and high-γ oscillations that appeared to be generated by distinct mechanisms. They occur at distinct phases of the breathing cycle and respond differently to changes in the excitatory-inhibitory balance of MCs (Lepousez and Lledo, 2013). Specific activation of GCL-ErbB4$^+$ neurons (at a minimal light intensity) increases only low-γ oscillation; however, stimulations at higher intensities also increase oscillations at theta and β frequencies and reduce high-γ oscillation, indicative of complex regulatory mechanisms for low- and high-γ oscillations. Beta oscillation is the least studied LFP band in the OB compared with theta and γ oscillations. The increased beta oscillation under intense light stimulation of the GCL-ErbB4$^+$ neurons could be an integrated activation of ErbB4$^+$ neurons in the EPL and even GL layers, both of which can strongly impact mitral cell activity (Kosaka and Kosaka, 2007; Huang et al., 2013; Kato et al., 2013; G. Liu et al., 2019). It is well established that centrifugal feedback to the OB plays a critical role in the generation of beta oscillation (Neville and Haberly, 2003; Martin et al., 2006; Martin and Ravel, 2014). Some projection neurons in the central brain may also express ErbB4 and consequently ChR2, therefore contributing to the generation of beta oscillation here.

Bulbar oscillations depend on recurrent and lateral excitation/inhibition mediated by the dendrodendritic reciprocal synapse between MCs and GABAergic interneurons (Kay et al., 2009; Martin and Ravel, 2014; Li and Cleland, 2017). In this special synapse, excitatory sensory inputs to MCs trigger glutamate release from their lateral dendrites, activating a large population of interneurons. These interneurons, in turn, inhibit MCs via dendritic GABA release (Yokoi et al., 1995; Nagayama et al., 2014). As typical PGs and GCs, GL-ErbB4$^+$ neurons could form dendrodendritic inhibitory synapses onto apical dendrites of MCs within the glomeruli. On the other hand, GCL-ErbB4$^+$ neurons could form dendrodendritic inhibitory synapses at secondary dendrites of MCs in the EPL. In accord with this speculation, bulbar oscillations were boosted by increasing GABA transmission from GL- and GCL-ErbB4$^+$ neurons by optogenetics, but attenuated by inhibiting GABA transmission from ErbB4$^+$ neurons by mutation or inhibition of ErbB4. Consistently, acute blockade of GABA transmission by local micro-infusion of GABA antagonists suppresses γ oscillations and impairs odor discrimination (Lepousez and Lledo, 2013).

In conclusion, our studies have revealed a novel bulbar interneuron network consisting of ErbB4$^+$ PGs and GCs. Synaptic transmission from ErbB4$^+$ neurons was dynamically regulated by the NRG1-ErbB4 signaling. Both the activity of ErbB4$^+$ neurons and the NRG1-ErbB4 signaling are critical to bulbar oscillations and olfaction. Given that *Nrg1* and *Erbb4* are risk genes for depression, bipolar disorder, and schizophrenia (Mei and Xiong, 2008; Shi et al., 2009; Mei and Nave, 2014; Howard et al., 2019), our study sheds light on potential mechanisms for associated olfactory malfunctions.

References

Ache BW, Young JM (2005) Olfaction: diverse species, conserved principles. Neuron 48:417–430.

Anton ES, Ghashghaei HT, Weber JL, McCann C, Fischer TM, Cheung ID, Gassmann M, Messing A, Klein R, Schwab MH, Lloyd KC, Lai C (2004) Receptor tyrosine kinase ErbB4 modulates neuroblast migration and placement in the adult forebrain. Nat Neurosci 7:1319–1328.

Aungst JL, Heyward PM, Puche AC, Karnup SV, Hayar A, Szabo G, Shipley MT (2003) Centre-surround inhibition among olfactory bulb glomeruli. Nature 426:623–629.

Bean JC, Lin TW, Sathyamurthy A, Liu F, Yin DM, Xiong WC, Mei L (2014) Genetic labeling reveals novel cellular targets of schizophrenia susceptibility gene: distribution of GABA and non-GABA ErbB4-positive cells in adult mouse brain. J Neurosci 34:13549–13566.

Bishop AC, Ubersax JA, Petsch DT, Matheos DP, Gray NS, Blethrow J, Shimizu E, Tsien JZ, Schultz PG, Rose MD, Wood JL, Morgan DO,

Shokat KM (2000) A chemical switch for inhibitor-sensitive alleles of any protein kinase. Nature 407:395–401.
Blatt M, Wiseman S, Domany E (1996) Superparamagnetic clustering of data. Phys Rev Lett 76:3251–3254.
Boyden ES, Zhang F, Bamberg E, Nagel G, Deisseroth K (2005) Millisecond-timescale, genetically targeted optical control of neural activity. Nat Neurosci 8:1263–1268.
Chen YJ, Zhang M, Yin DM, Wen L, Ting A, Wang P, Lu YS, Zhu XH, Li SJ, Wu CY, Wang XM, Lai C, Xiong WC, Mei L, Gao TM (2010) ErbB4 in parvalbumin-positive interneurons is critical for neuregulin 1 regulation of long-term potentiation. Proc Natl Acad Sci USA 107:21818–21823.
Christie JM, Schoppa NE, Westbrook GL (2001) Tufted cell dendrodendritic inhibition in the olfactory bulb is dependent on NMDA receptor activity. J Neurophysiol 85:169–173.
Cleland TA, Linster C (2012) On-center/inhibitory-surround decorrelation via intraglomerular inhibition in the olfactory bulb glomerular layer. Front Integr Neurosci 6:5.
Del Pino I, Garcia-Frigola C, Dehorter N, Brotons-Mas JR, Alvarez-Salvado E, Martinez de Lagran M, Ciceri G, Gabaldon MV, Moratal D, Dierssen M, Canals S, Marin O, Rico B (2013) Erbb4 deletion from fast-spiking interneurons causes schizophrenia-like phenotypes. Neuron 79:1152–1168.
Dong HW, Hayar A, Ennis M (2007) Activation of group I metabotropic glutamate receptors on main olfactory bulb granule cells and periglomerular cells enhances synaptic inhibition of mitral cells. J Neurosci 27:5654–5663.
Economo MN, Hansen KR, Wachowiak M (2016) Control of mitral/tufted cell output by selective inhibition among olfactory bulb glomeruli. Neuron 91:397–411.
Figueres-Onate M, Gutierrez Y, Lopez-Mascaraque L (2014) Unraveling Cajal's view of the olfactory system. Front Neuroanat 8:55.
Firestein S (2001) How the olfactory system makes sense of scents. Nature 413:211–218.
Fukunaga I, Herb JT, Kollo M, Boyden ES, Schaefer AT (2014) Independent control of gamma and theta activity by distinct interneuron networks in the olfactory bulb. Nat Neurosci 17:1208–1216.
Ghashghaei HT, Weber J, Pevny L, Schmid R, Schwab MH, Lloyd KC, Eisenstat DD, Lai C, Anton ES (2006) The role of neuregulin-ErbB4 interactions on the proliferation and organization of cells in the subventricular zone. Proc Natl Acad Sci USA 103:1930–1935.
Gire DH, Schoppa NE (2009) Control of on/off glomerular signaling by a local GABAergic microcircuit in the olfactory bulb. J Neurosci 29:13454–13464.
Howard DM, et al. (2019) Genome-wide meta-analysis of depression identifies 102 independent variants and highlights the importance of the prefrontal brain regions. Nat Neurosci 22:343–352.
Hu J, Zhong C, Ding C, Chi Q, Walz A, Mombaerts P, Matsunami H, Luo M (2007) Detection of near-atmospheric concentrations of CO_2 by an olfactory subsystem in the mouse. Science 317:953–957.
Huang L, Garcia I, Jen HI, Arenkiel BR (2013) Reciprocal connectivity between mitral cells and external plexiform layer interneurons in the mouse olfactory bulb. Front Neural Circuits 7:32.
Huang YZ, Won S, Ali DW, Wang Q, Tanowitz M, Du QS, Pelkey KA, Yang DJ, Xiong WC, Salter MW, Mei L (2000) Regulation of neuregulin signaling by PSD-95 interacting with ErbB4 at CNS synapses. Neuron 26:443–455.
Imai T (2014) Construction of functional neuronal circuitry in the olfactory bulb. Semin Cell Dev Biol 35:180–188.
Isaacson JS, Strowbridge BW (1998) Olfactory reciprocal synapses: dendritic signaling in the CNS. Neuron 20:749–761.
Kato HK, Gillet SN, Peters AJ, Isaacson JS, Komiyama T (2013) Parvalbumin-expressing interneurons linearly control olfactory bulb output. Neuron 80:1218–1231.
Kay LM, Beshel J, Brea J, Martin C, Rojas-Libano D, Kopell N (2009) Olfactory oscillations: the what, how and what for. Trends Neurosci 32:207–214.
Kiyokage E, Pan YZ, Shao Z, Kobayashi K, Szabo G, Yanagawa Y, Obata K, Okano H, Toida K, Puche AC, Shipley MT (2010) Molecular identity of periglomerular and short axon cells. J Neurosci 30:1185–1196.
Kosaka K, Kosaka T (2007) Chemical properties of type 1 and type 2 periglomerular cells in the mouse olfactory bulb are different from those in the rat olfactory bulb. Brain Res 1167:42–55.
Lepousez G, Lledo PM (2013) Odor discrimination requires proper olfactory fast oscillations in awake mice. Neuron 80:1010–1024.
Li G, Cleland TA (2017) A coupled-oscillator model of olfactory bulb gamma oscillations. PLoS Comput Biol 13:e1005760.
Liu G, Froudarakis E, Patel JM, Kochukov MY, Pekarek B, Hunt PJ, Patel M, Ung K, Fu CH, Jo J, Lee HK, Tolias AS, Arenkiel BR (2019) Target specific functions of EPL interneurons in olfactory circuits. Nat Commun 10:3369.
Liu X, Bates R, Yin DM, Shen C, Wang F, Su N, Kirov SA, Luo Y, Wang JZ, Xiong WC, Mei L (2011) Specific regulation of NRG1 isoform expression by neuronal activity. J Neurosci 31:8491–8501.
Lledo PM, Merkle FT, Alvarez-Buylla A (2008) Origin and function of olfactory bulb interneuron diversity. Trends Neurosci 31:392–400.
Madisen L, Zwingman TA, Sunkin SM, Oh SW, Zariwala HA, Gu H, Ng LL, Palmiter RD, Hawrylycz MJ, Jones AR, Lein ES, Zeng H (2010) A robust and high-throughput Cre reporting and characterization system for the whole mouse brain. Nat Neurosci 13:133–140.
Martin C, Ravel N (2014) Beta and gamma oscillatory activities associated with olfactory memory tasks: different rhythms for different functional networks? Front Behav Neurosci 8:218.
Martin C, Gervais R, Messaoudi B, Ravel N (2006) Learning-induced oscillatory activities correlated to odour recognition: a network activity. Eur J Neurosci 23:1801–1810.
McQuiston AR, Katz LC (2001) Electrophysiology of interneurons in the glomerular layer of the rat olfactory bulb. J Neurophysiol 86:1899–1907.
Mei L, Xiong WC (2008) Neuregulin 1 in neural development, synaptic plasticity and schizophrenia. Nat Rev Neurosci 9:437–452.
Mei L, Nave KA (2014) Neuregulin-ERBB signaling in the nervous system and neuropsychiatric diseases. Neuron 83:27–49.
Miyamichi K, Shlomai-Fuchs Y, Shu M, Weissbourd BC, Luo L, Mizrahi A (2013) Dissecting local circuits: parvalbumin interneurons underlie broad feedback control of olfactory bulb output. Neuron 80:1232–1245.
Mori K, Nagao H, Yoshihara Y (1999) The olfactory bulb: coding and processing of odor molecule information. Science 286:711–715.
Mukai J, Tamura M, Fenelon K, Rosen AM, Spellman TJ, Kang R, MacDermott AB, Karayiorgou M, Gordon JA, Gogos JA (2015) Molecular substrates of altered axonal growth and brain connectivity in a mouse model of schizophrenia. Neuron 86:680–695.
Nagayama S, Homma R, Imamura F (2014) Neuronal organization of olfactory bulb circuits. Front Neural Circuits 8:98.
Najac M, Sanz Diez A, Kumar A, Benito N, Charpak S, De Saint Jan D (2015) Intraglomerular lateral inhibition promotes spike timing variability in principal neurons of the olfactory bulb. J Neurosci 35:4319–4331.
Neville KR, Haberly LB (2003) Beta and gamma oscillations in the olfactory system of the urethane-anesthetized rat. J Neurophysiol 90:3921–3930.
Oppenheim AV, Schafer RW, Buck JR (1999) Discrete-time signal processing, Ed 2. Hoboken, NJ: Prentice Hall.
Pinching AJ, Powell TP (1971) The neuropil of the glomeruli of the olfactory bulb. J Cell Sci 9:347–377.
Pollock GS, Franceschini IA, Graham G, Marchionni MA, Barnett SC (1999) Neuregulin is a mitogen and survival factor for olfactory bulb ensheathing cells and an isoform is produced by astrocytes. Eur J Neurosci 11:769–780.
Ressler KJ, Sullivan SL, Buck LB (1994) Information coding in the olfactory system: evidence for a stereotyped and highly organized epitope map in the olfactory bulb. Cell 79:1245–1255.
Schoppa NE (2006) Synchronization of olfactory bulb mitral cells by precisely timed inhibitory inputs. Neuron 49:271–283.
Schoppa NE, Kinzie JM, Sahara Y, Segerson TP, Westbrook GL (1998) Dendrodendritic inhibition in the olfactory bulb is driven by NMDA receptors. J Neurosci 18:6790–6802.
Shi J, et al. (2009) Common variants on chromosome 6p22.1 are associated with schizophrenia. Nature 460:753–757.
Sigurdsson T, Stark KL, Karayiorgou M, Gogos JA, Gordon JA (2010) Impaired hippocampal-prefrontal synchrony in a genetic mouse model of schizophrenia. Nature 464:763–767.

Spellman T, Rigotti M, Ahmari SE, Fusi S, Gogos JA, Gordon JA (2015) Hippocampal-prefrontal input supports spatial encoding in working memory. Nature 522:309–314.

Tan Z, Robinson HL, Yin DM, Liu Y, Liu F, Wang H, Lin TW, Xing G, Gan L, Xiong WC, Mei L (2018) Dynamic ErbB4 activity in hippocampal-prefrontal synchrony and top-down attention in rodents. Neuron 98:380–393.e384.

Tidcombe H, Jackson-Fisher A, Mathers K, Stern DF, Gassmann M, Golding JP (2003) Neural and mammary gland defects in ErbB4 knockout mice genetically rescued from embryonic lethality. Proc Natl Acad Sci USA 100:8281–8286.

Toida K, Kosaka K, Heizmann CW, Kosaka T (1994) Synaptic contacts between mitral/tufted cells and GABAergic neurons containing calcium-binding protein parvalbumin in the rat olfactory bulb, with special reference to reciprocal synapses between them. Brain Res 650:347–352.

Toida K, Kosaka K, Heizmann CW, Kosaka T (1996) Electron microscopic serial-sectioning/reconstruction study of parvalbumin-containing neurons in the external plexiform layer of the rat olfactory bulb. Neuroscience 72:449–466.

Toida K, Kosaka K, Heizmann CW, Kosaka T (1998) Chemically defined neuron groups and their subpopulations in the glomerular layer of the rat main olfactory bulb: III. Structural features of calbindin D28K-immunoreactive neurons. J Comp Neurol 392:179–198.

Urban NN, Sakmann B (2002) Reciprocal intraglomerular excitation and intra- and interglomerular lateral inhibition between mouse olfactory bulb mitral cells. J Physiol 542:355–367.

Wang YY, Zhao B, Wu MM, Zheng XL, Lin L, Yin DM (2021) Overexpression of neuregulin 1 in GABAergic interneurons results in reversible cortical disinhibition. Nat Commun 12:278.

Woo RS, Li XM, Tao Y, Carpenter-Hyland E, Huang YZ, Weber J, Neiswender H, Dong XP, Wu J, Gassmann M, Lai C, Xiong WC, Gao TM, Mei L (2007) Neuregulin-1 enhances depolarization-induced GABA release. Neuron 54:599–610.

Yokoi M, Mori K, Nakanishi S (1995) Refinement of odor molecule tuning by dendrodendritic synaptic inhibition in the olfactory bulb. Proc Natl Acad Sci USA 92:3371–3375.